Wavy regimes of film flow down a fiber

Christian Ruyer-Quil

UPMC Université Paris 06, Univ Paris-Sud, CNRS, Lab FAST, Bat 502, Campus Université, Orsay, F-91405, France

Serafim Kalliadasis

Department of Chemical Engineering, Imperial College London, London SW7 2AZ, United Kingdom

We consider axisymmetric traveling waves propagating on the gravity-driven flow of a liquid down a vertical fiber. Our starting point is the two-equation model for the flow derived in the study by Ruyer-Quil *et al.* [J. Fluid Mech. **603**, 431 (2008)]. The speed, amplitude, and shape of the traveling waves are obtained for a wide range of parameters by using asymptotic analysis and elements from dynamical systems theory. Four different regimes are identified corresponding to the predominance of four different physical effects: advection by the flow, azimuthal curvature, inertia, and viscous dispersion. Construction of the traveling-wave branches of solutions reveals complex transitions from one regime to another. A phase diagram of the different regimes in the parameter space is constructed.

PACS number(s): 47.15.gm, 47.20.Ma, 47.35.Fg, 47.10.Fg

I. INTRODUCTION

A liquid film flowing down a vertical fiber is often encountered in a wide variety of technological applications such as condensers, emergency cooling of nuclear fuel rods, and optical fiber coating. It can also serve as a simple prototype for the study of wave instabilities and transitions in open flow hydrodynamic and other nonlinear systems. As a consequence, this problem has been an active topic of both experimental and theoretical research, especially over the past two decades [1].

Experimental studies have revealed a complex wave dynamics dominated by axisymmetric and localized teardroplike structures which continuously interact with each other [2–6]. These structures are robust as they propagate over long distances without changing their speed or shape significantly; they are also separated by portions of nearly flat film, and they can be referred to as traveling waves. When the portions of nearly flat film between these structures are much longer than their characteristic length, the structures can be referred to as solitary waves. The formation of solitary and traveling waves results from the interplay between two different instability mechanisms: (i) the classical instability of a liquid film flowing down an inclined planar wall prompted by inertia effects, a mode initially characterized experimentally and theoretically by Kapitza and his son [7]; (ii) the interfacial instability of a liquid cylinder, considered first in experiments by Plateau and theoretically explained by Lord Rayleigh [8,9]. These two mechanisms are hereinafter referred to as the K and RP modes of instability, respectively.

The experimental study by Duprat *et al.* [6], provided reports on the traveling waves' characteristics, namely, shape, speed, and amplitude, for very viscous fluids. The parameter values in the experiments were chosen in order to investigate the interplay of the K and RP modes on the waves; thus, the study by Duprat *et al.* [6] completed the flow regime portrait obtained by Kliakhandler [3] for very viscous fluids but in the inertialess limit. Regular wave trains were generated by means of a periodic forcing at the inlet. Two flow regimes were identified. For thin fibers and/or small flow rates, the RP mode is dominant and the solitary waves resemble beads or sliding drops whose shape is affected by gravity. At the same time, the flow field in a frame moving with the beads is characterized by recirculation zones within the beads. When closed streamlines exist in the moving frame, a fluid particle is trapped in both moving and laboratory frames. Hence, the beads transport the trapped fluid mass downstream. For these reasons, we refer to the flow regime observed for thin fibers and/or small flow rates, as the *droplike regime*.

For thick fibers and/or large flow rates, the K mode is dominant and a steepening of the wave front is observed with an increase of the wave amplitude. Mass transport is not observed in this regime except for a few cases corresponding to the largest waves. We refer to this regime as the *wavelike regime*. We can conjecture that the onset of recirculation zones in the wavelike regime is a signature of the increased prevalence of the K mode. Eventually, we observe a transition from the *drag-gravity* regime, where inertia plays a perturbative role, to the *drag-inertia* regime, where inertia effects become dominant. Similar regimes and a transition between the two as inertia effects increase were first observed in the planar case [10,11].

At the theoretical front, a number of modeling approaches have been proposed within the framework of the long-wave approximation of the Navier-Stokes equations and associated wall and free-surface boundary conditions [3,4,12–17]: The basic assumption of this approximation is that of slow spatial and time modulations of the film thickness motivating the introduction of a formal perturbation parameter, the "long-wave" or "film parameter" ϵ measuring such modulations. Perturbation expansions in terms of this parameter then lead to simplifications of the governing equations and boundary conditions. Additional assumptions lead to further simplifications, that is, small film thickness h in comparison to the fiber radius R or negligible inertia. The resulting models are either single evolution equations for the film thickness h, for example, the model by Frenkel [12] based on the long-wave approximation only, or systems of two coupled evolution equations for the film thickness h and streamwise flow rate

q which combine the long-wave approximation and other approaches, for example, the model by Trifonov [13] based on the "integral-boundary-layer" approximation and the more recent model by Novbari and Oron [17] based on an "energy integral" method.

It should be noted that all the above studies neglected the second-order viscous terms originating from the streamwise momentum equation (streamwise viscous diffusion) and tangential stress balance (second-order contributions to the tangential stress at the free surface). The recent study by Ruyer-Quil *et al.* [18] formulated a two-evolution equation model for h and q that took into account the second-order viscous terms but also included inertia and was not limited to small aspect ratios h/R. The model was based on a combination of the long-wave approximation and a weighted-residuals approach using appropriate polynomial test functions for the velocity field—a "weighted-residuals integral boundary layer" (WRIBL) model following the terminology introduced by Oron *et al.* [19]. It should be noted that the WRIBL model is consistent [20] at $O(\epsilon)$ for the inertial terms and at $O(\epsilon^2)$ for the remaining contributions, whereas the models obtained by Trifonov [13] and Novbari and Oron [17] are not consistent at $O(\epsilon)$. Furthermore, the study by Duprat *et al.* [21] compared the wave trains generated experimentally by periodic forcing at the inlet to the traveling-wave solutions of the WRIBL model showing remarkable agreement in all cases, thus validating experimentally the model.

As was shown in Ref. [18], the second-order viscous terms have a dispersive effect on the speed of the linear waves (they introduce a wave-number dependence on the speed) and hence we refer to this effect as *viscous dispersion*. Viscous dispersion influences the shape of the capillary ripples in front of a solitary hump, more specifically, the amplitude and frequency of the capillary ripples, an effect which is amplified as the Reynolds number is increased. Hence, viscous dispersion is, in fact, a linear effect, but interestingly it can have some crucial consequences on the nonlinear dynamics of the film and the wave-selection process in the spatiotemporal evolution. These points have been analyzed in detail in the recent work by Pradas *et al.* [22] on coherent structures interaction on falling films on planar walls and the influence of viscous dispersion on interaction. Their analysis was based on the weighted-residuals models obtained in Refs. [23–25].

The main aim of the present study is to characterize theoretically the solitary and traveling waves propagating down the fiber within the framework of the WRIBL model. A first stab to the investigation of the traveling-wave solutions of the WRIBL model was the recent study by Ruyer-Quil *et al.* ([18], Sect. 6). In this study traveling-wave solutions were constructed numerically and were favorably compared to the experiments by Kliakhandler *et al.* [3], as noted earlier. Here we undertake an asymptotic analysis of the governing equations for solitary and traveling waves in various limiting cases. We also obtain both numerically and asymptotically static drops in the droplike regime. Furthermore, by using elements from dynamical systems theory, we provide a detailed and systematic parametric study of the waves' speed, shape, and amplitude; that is, we construct bifurcation diagrams for their speed as a function of pertinent parameters, as well as obtain ranges in the parameter space for which the K or

RP modes of instability, prompted by inertia and azimuthal curvature, respectively, are dominant. We scrutinize the four different regimes described earlier (droplike, wavelike, drag-gravity, drag-inertia) and provide detailed phase diagrams and corresponding regime maps for very viscous and less viscous fluids, thus providing a deeper understanding of the problem, as well as new insights and also completing the flow regime diagram provided in [6] for viscous fluids.

Section II introduces the pertinent nondimensionalization and the WRIBL model. Solitary-wave solutions are constructed in Sec. III. Asymptotic limits for small and large values of the pertinent parameters are analyzed in Sec. IV. Traveling waves corresponding to the experimental conditions considered in Refs. [3,5] are next discussed in Sec. V. Section VI presents a phase diagram of the different regimes. Finally, a summary of our findings and concluding remarks is offered in Sec. VII.

II. FORMULATION

A. Natural set of parameters

Consider a film flowing down a vertical cylinder under the action of gravity. The liquid has dynamic and kinematic viscosity, μ and ν, respectively, density ρ and surface tension σ. The flow is assumed to remain axisymmetric. $\bar{r}$, $\bar{x}$, $\bar{u}$, and $\bar{t}$ denote the radial, pointing outward from the fiber centerline coordinate, the axial coordinate oriented along gravity, the axial velocity distribution and time, respectively (bars are used to distinguish dimensional from dimensionless quantities unless the distinction is unnecessary). From simple physical considerations and without prior knowledge of the specific details of the system, the following scales can be readily identified: the fiber radius $\bar{R}$, the Nusselt thickness $\bar{h}_{\mathrm{N}}$ of the uniformly coated film, the length and time scales, $l_\nu = \nu^{2/3} g^{-1/3}$ and $t_\nu = \nu^{1/3} g^{-1/3}$, based on gravity and viscosity (making explicit the balance between gravity and viscous forces giving rise to the Nusselt flat-film solution), and the capillary length $l_c = \sqrt{\sigma/(\rho g)}$.

A first set of pertinent dimensionless groups arises from these scales. The aspect ratio,

$$\tilde{\alpha} \equiv \bar{h}_{\mathrm{N}}/\bar{R}, \tag{1a}$$

which assesses azimuthal curvature effects at the scale of the film, the Goucher number [26],

$$\mathrm{Go} \equiv \bar{R}/l_c, \tag{1b}$$

which compares azimuthal and axial surface tension effects, and the Kapitza number,

$$\Gamma \equiv \sigma/(\rho \nu^{4/3} g^{1/3}) = (l_c/l_\nu)^2, \tag{1c}$$

comparing surface tension and viscosity. Useful combinations of these parameters are $h_{\mathrm{N}} \equiv \bar{h}_{\mathrm{N}}/l_\nu$ and $\bar{h}_{\mathrm{N}}/l_c$. The former compares the film thickness to the gravity-viscous length scale and, indirectly, inertia and viscosity since the Nusselt base flow is the result of the balance of gravity and viscosity. The latter, $\bar{h}_{\mathrm{N}}/l_c$ is related to the Bond number $\mathrm{Bo} = \rho g \bar{h}_{\mathrm{N}}^2/\sigma = (\bar{h}_{\mathrm{N}}/l_c)^2$ comparing surface tension and gravity at the scale of the film.

The advantage of the set of parameters $\tilde{\alpha}$, Go, and Γ is that when the geometry and the working fluid are fixed, the

TABLE I. Fluid properties, capillary length l_c, gravity-viscous length l_v, and Kapitza number used in the present study. The data for silicon oil v50 and castor oil have been taken from [3,5].

	ν (mm^2 s^{-1})	ρ (kg m^{-3})	σ (mN m^{-1})	l_c (mm)	l_v (mm)	Γ
Water	1	998	72.5	2.7	0.047	3376
Rhodorsil silicon oil v50	50	963	20.8	1.5	0.63	5.48
Castor oil	440	961	31	1.8	2.7	0.45
Rhodorsil silicon oil v1000	1000	980	21.1	1.5	4.7	0.10

Goucher and the Kapitza numbers Go and Γ are constant and the only free parameter is $\tilde{\alpha}$. From an experimental point of view, $\tilde{\alpha}$ can be varied independently by varying the inlet flow rate. The Kapitza number Γ is entirely defined by the fluid properties independently of the flow characteristics, whereas the Goucher number Go can be easily varied by replacing the fiber. Hence, the parameters $\tilde{\alpha}$, Go, and Γ can therefore be viewed as "natural" for the fiber problem, and we systematically recast our results in terms of these parameters.

Table I gives the physical properties of four different fluids of increasing viscosities commonly used in experiments and corresponding to a wide range of Kapitza numbers together with the corresponding capillary lengths and viscous-gravity length scales. For simplicity, our results will be presented for the Kapitza numbers listed in Table I.

B. WRIBL model

We now adapt Shkadov's scaling [27] and introduce different length scales for the streamwise (axial) and radial directions. The length scale in the radial direction is the Nusselt thickness $\bar{h}_N$, whereas the length scale in the streamwise

direction is chosen as $\kappa \bar{h}_N$ defined by the balance of the streamwise pressure gradient induced by capillarity, $\propto \sigma \partial_{xxx} h$, and gravity acceleration, ρg, which gives $\kappa = [\sigma/(\rho g \bar{h}_N^2)]^{1/3} = (l_c/\bar{h}_N)^{2/3}$. The time scale is defined with reference to the Nusselt solution of uniform thickness (a result of the balance of gravity and viscosity). The volumetric flow rate per unit length of circumference, $q_N = R^{-1} \int_R^{R+h_N} u\, r\, dr$, of a film of constant thickness $\bar{h}_N$ is given by

$$\bar{q}_N \equiv \frac{g \bar{h}_N^3}{3\nu} \phi(\tilde{\alpha}), \tag{2}$$

where ϕ is a geometric factor defined in Eq. (A1a) and measures the deviation of the flow-rate-to-thickness relation from the cubic dependency corresponding to the planar geometry [$\phi(0) = 1$]. Similarly to the streamwise length scale, the time scale is stretched by a factor κ and thus defined as $3\kappa \bar{h}_N^2/\bar{q}_N = \nu\kappa/[g\bar{h}_N \phi(\tilde{\alpha})]$.

Our basic equations for the analysis to follow are the WRIBL model obtained in Ref. [18], a set of two evolution equations for the local film thickness $h(x,t)$, and the local flow rate $q(x,t) \equiv R^{-1} \int_R^{R+h(x,t)} u\, r\, dr$. For the sake of clarity and completeness we rewrite the WRIBL model here,

$$\partial_t h = -\frac{1}{1 + \tilde{\alpha} h} \partial_x q, \tag{3a}$$

$$\delta \partial_t q = \delta \left[-F(\tilde{\alpha} h) \frac{q}{h} \partial_x q + G(\tilde{\alpha} h) \frac{q^2}{h^2} \partial_x h \right] + \frac{I(\tilde{\alpha} h)}{\phi(\tilde{\alpha})} \left[-\frac{3\phi(\tilde{\alpha})}{\phi(\tilde{\alpha} h)} \frac{q}{h^2} + h \left\{ 1 + \partial_{xxx} h + \frac{\beta}{(1 + \tilde{\alpha} h)^2} \partial_x h \right. \right.$$
$$\left. \left. - \frac{1}{2} \partial_x \left(\frac{\tilde{\alpha}}{1 + \tilde{\alpha} h} (\partial_x h)^2 \right) \right\} \right] + \eta \left[J(\tilde{\alpha} h) \frac{q}{h^2} (\partial_x h)^2 - K(\tilde{\alpha} h) \frac{\partial_x q\, \partial_x h}{h} - L(\tilde{\alpha} h) \frac{q}{h} \partial_{xx} h + M(\tilde{\alpha} h) \partial_{xx} q \right], \tag{3b}$$

in terms of the Shkadov scaling, where ϕ, F, G, I, J, K, L, and M are functions of the aspect ratio $\tilde{\alpha}$ given in Appendix A. Equation (3a) is the (exact) dimensionless mass balance, whereas (3b) is the streamwise momentum equation averaged across the film with a weighted-residuals approach.

Shkadov's scales introduce three new dimensionless groups besides the aspect ratio $\tilde{\alpha} = h_N/R$, a "reduced Reynolds number,"

$$\delta \equiv 3\bar{q}_N/(\nu\kappa) = \phi(\tilde{\alpha})\Gamma^{3/2} (\tilde{\alpha} \text{Go})^{11/3}, \tag{4a}$$

which compares inertia and the viscous drag at the scale $\kappa \bar{h}_N$ introduced by the balance of gravity and capillarity, a

streamwise "viscous dispersion parameter,"

$$\eta \equiv 1/\kappa^2 = (\bar{h}_N/l_c)^{4/3} = (\tilde{\alpha} \text{Go})^{4/3}, \tag{4b}$$

and the dimensionless group,

$$\beta \equiv \tilde{\alpha}^2/\eta = \tilde{\alpha}^{2/3} \text{Go}^{-4/3}, \tag{4c}$$

which is a combination of $\tilde{\alpha}$ and η and compares azimuthal to axial surface tension effects. We have made explicit in Eq. (4) the relations of δ, η, and β to the "natural" parameters $\tilde{\alpha}$, Go, and Γ. Notice that all second-order viscous-dispersion terms are gathered in the last row of (3b) and are multiplied by η. Let us also recall the usual definition of the Reynolds number based on the flow rate, Re $= \bar{q}_N/\nu = h_N^3 \phi(\tilde{\alpha})/3$, where again $h_N = \bar{h}_N/l_v$. δ and Re are thus related one to another by $\delta = 3\text{Re}/\kappa$.

Let us emphasize that the WRIBL model has been validated in Refs. [6,18] through direct comparisons to the experiments in Refs. [3,5,6] as noted in Sec. I [for both very viscous and less viscous liquids (castor oil and silicon oil v50, see Table I) and a wide range of the parameters ($0.15 \leqslant \mathrm{Go} \leqslant 1$, $0.5 \leqslant \tilde{\alpha} \leqslant 4.5$, and $0.05 \leqslant \delta \leqslant 4$)].

The advantage of Shkadov's scaling stems from (i) the direct reference to the Nusselt uniform film flow that simplifies the comparisons between solutions, with the Nusselt solution corresponding to constant values of the film thickness and flow rates $h = 1$ and $q = 1/3$; (ii) the association of a single parameter to each physical effect affecting the balance of the different forces: Inertia (δ), azimuthal surface tension (β), viscous dispersion (η), and geometry ($\tilde{\alpha}$).

To end this section let us point out one apparent drawback of the Shkadov scaling, namely the divergence of the dimensionless parameter $\beta = \tilde{\alpha}^2/\eta$ as the viscous dispersion parameter goes to zero for $\tilde{\alpha} = O(1)$. The divergence of β signals that the typical length of a wave is not determined by the balance of gravitational and axial capillary forces, as assumed in Shkadov's scaling, but rather by the balance of axial and azimuthal capillary forces, in which case the typical curvatures of the beads in the azimuthal and axial directions must coincide. The beads have thus a droplike rounded shape, the long-wave approximation starts to be violated, and the viscous dispersion effects cannot be *a priori* discarded as in the planar case. Considering droplike beads (see Sec. IV A) it can thus be useful to adopt a scaling based on the radius $\bar{R}$ of the fiber, which gives the time scale $\nu/(g\bar{R})$. This scaling introduces a Galilei number, $\mathrm{Ga} \equiv g\bar{R}^3/\nu^2 = \mathrm{Go}^3 \Gamma^{3/2}$.

C. Surface equations and saturation numbers

Neglecting inertia and viscous dispersion, Craster and Matar [4] formulated a single evolution equation for the film thickness h, the Craster and Matar (CM) equation,

$$
\partial_t \left(h + \frac{\tilde{\alpha}}{2} h^2 \right)
+ \partial_x \left[\frac{h^3}{3} \frac{\phi(\tilde{\alpha}h)}{\phi(\tilde{\alpha})} \left(1 + \frac{\beta}{(1+\tilde{\alpha}h)^2} \partial_x h + \partial_{xxx} h \right) \right] = 0. \quad (5)
$$

For sufficiently thin films, that is, $\tilde{\alpha} \to 0$, we obtain from (5)

$$
\partial_t h + \partial_x \left[\frac{h^3}{3} \left(1 + \beta \partial_x h + \partial_{xxx} h \right) \right] = 0, \quad (6)
$$

which is the equation derived initially by Frenkel [12] (see also [14]). Equations (5) and (6) are the simplest evolution equations balancing all relevant physical effects, gravity, viscous drag, surface tension, and the fiber curvature. They are equations for the free surface $h(x,t)$ only and, following the terminology introduced by Ooshida [10], we refer to them as *surface equations*.

The CM equation offers a simple prototype for the flow, easily amenable to mathematical and numerical scrutiny for which the set of parameters is reduced to only two: $\tilde{\alpha}$ and β (or equivalently Go). It can be obtained asymptotically from (3) in the limit $\delta \to 0$ and $\eta \to 0$ when the nonlinear term $-1/2\partial_x[\tilde{\alpha}/(1+\tilde{\alpha}h)(\partial_x h)^2]$ of the azimuthal curvature gradient is omitted. Yet, as already stated, $\tilde{\alpha} = O(1)$ implies

that β diverges to infinity and therefore that second-order viscous dispersive terms cannot be *a priori* discarded and that the long-wave assumption is invalid. By contrast, the derivation of the Frenkel's equation (6) can be obtained in the distinguished limit $\tilde{\alpha} \to 0$, $\eta \to 0$, and $\beta = \tilde{\alpha}^2/\eta = O(1)$. Nevertheless, comparisons of the solutions to the CM equation to the experiments show good agreement [18,21].

Using the surface equation (6), Kalliadasis and Chang [14] and Chang and Demekhin [28] analyzed the mechanism of the formation of drops observed by Quéré [2] when a fiber or wire is drawn out of a liquid bath. Quéré observed suppression of the RP mode for sufficiently small coating films. More specifically, below a certain critical thickness the film deposited on the wire develops small-amplitude interfacial waves with the flow preventing their growth into drops (such drops would always be observed when the wire is horizontal, as the suppression of the RP mode induced by the flow is absent in this case). On the other hand, beyond the critical film thickness growth of the interfacial waves into drops was observed. Kalliadasis and Chang [14] found that the amplitude of the solitary-wave solutions to (6) diverges or "blows-up" for β larger than a critical value $\beta_c = 1.413$, which closely corresponds to the formation of drops in Quéré's experiments. These authors also performed an analytical construction of the solitary waves for $\beta \to \beta_c$ using matched asymptotic expansions. They showed that drop formation results from the inability of the flow advection to saturate the instability growth through a nonlinear saturation mechanism.

The advection and the growth of the instability can be compared through the definition of the advection time τ_a of an interfacial structure over its length and the definition of a typical time of growth of the structure τ_g as the inverse of the maximum temporal growth rate. Based on the Frenkel equation (6), the stability analysis of the uniform film leads to the dispersion relation

$$
\omega = k + \frac{\mathrm{i}k^2}{3}(\beta - k^2), \quad (7)
$$

which governs infinitesimal perturbations around the base Nusselt flow of wave number k and angular frequency ω. τ_a and τ_g are thus defined as $1/\omega_r(k = k_{\max})$ and $\tau_g = 1/\omega_i(k = k_{\max})$, where ω_r and ω_i refer to the real and imaginary part of the temporal mode ($k \in \mathbb{R}$), respectively, the maximum of the temporal growth rate ω_i being reached at $k = k_{\max}$. Based on (7) the ratio τ_a/τ_g reads

$$
\tau_a/\tau_g = \omega_i/\omega_r|_{k=\sqrt{\beta/2}} = \frac{\beta^2}{12}\sqrt{\frac{2}{\beta}} = \frac{\sqrt{2}}{12}\beta^{3/2}, \quad (8)
$$

the maximum temporal growth rate being obtained at $k_{\max} = \sqrt{\beta/2}$ (see [18] for details). Therefore, β compares τ_a to τ_g. For $\beta < \beta_c$, the instability growth is slower than the advection by the flow. The same mechanism is also in play in the saturation of the drops though it is then strongly nonlinear. For these reasons, we refer to β as a *saturation number*, a term that was first introduced in Ref. [6].

TABLE II. Summary of the different parameters defined in Eqs. (1), (4), and (10). The last row recalls the expressions of the reduced parameters and saturation numbers as functions of the natural parameters. $l_c = \sqrt{\sigma/(\rho g)}$ and $l_v = \nu^{2/3} g^{-1/3}$ refer to the capillary length and viscous-gravity length scale, respectively. The scale ratio κ is defined as $\kappa = (l_c/\bar{h}_N)^{2/3}$ and the kinematic wave speed c_k is a function of $\tilde{\alpha}$ given in Eq. (11).

Natural			Reduced		Saturation numbers	
$\tilde{\alpha}$	Go	Γ	δ	η	β	$\beta^{\star}$
$\dfrac{\bar{h}_N}{\bar{R}}$	$\dfrac{\bar{R}}{l_c}$	$\left(\dfrac{l_c}{l_v}\right)^2$	$\dfrac{3\mathrm{Re}}{\kappa}$	$\dfrac{1}{\kappa^2}$	$\dfrac{\tilde{\alpha}^2}{\eta}$	$\dfrac{\beta}{c_k^{2/3}(1+\tilde{\alpha})^{8/3}}$
			$\phi(\tilde{\alpha})\Gamma^{3/2}(\tilde{\alpha}\mathrm{Go})^{11/3}$	$(\tilde{\alpha}\mathrm{Go})^{4/3}$	$\dfrac{\tilde{\alpha}^{2/3}}{\mathrm{Go}^{4/3}}$	

From the CM equation (5), we get

$$\tau_a/\tau_g = \omega_i/\omega_r|_{k=k_{RP}/\sqrt{2}} \tag{9a}$$

$$= \frac{\beta^2}{12(1+\tilde{\alpha})^5}\frac{\sqrt{2}(1+\tilde{\alpha})}{c_k\sqrt{\beta}} = \frac{\sqrt{2}}{12}(\beta^{\star})^{3/2}, \tag{9b}$$

where $k_{RP} \equiv \sqrt{\beta}/(1+\tilde{\alpha})$ corresponds to the marginal stability condition and the composite parameter $\beta^{\star}$ is defined as [5,18]

$$\beta^{\star} = \beta c_k^{-2/3}(1+\tilde{\alpha})^{-8/3}. \tag{10}$$

$c_k = \lim_{k\to 0} \omega/k$ is the speed at which infinitesimal deformations of infinite lengths are kinematically transported by the flow, or *kinematic wave speed*:

$$c_k = \frac{1}{1+\tilde{\alpha}}\left[1 + \frac{\tilde{\alpha}\phi'(\tilde{\alpha})}{3\phi(\tilde{\alpha})}\right] \tag{11a}$$

$$= \frac{8(b-1)(2\log(b)b^2 - b^2 + 1)}{3(4\log(b)b^4 - 3b^4 + 4b^2 - 1)}, \tag{11b}$$

with $b = 1 + \tilde{\alpha}$.

Since $c_k(\tilde{\alpha} = 0) = 1$, $\lim_{\tilde{\alpha}\to 0}\beta^{\star} = \beta$. In this limit the Frenkel equation (6) limited to very thin films ($\tilde{\alpha} \ll 1$) applies and $\beta^{\star}$ is a generalization of the saturation number β to film flows with thicknesses comparable to the fiber radius.

Table II regroups the main parameters of our study along with the definition of the saturation numbers. As already stated, experimental conditions are well represented by the natural parameters (they can be independently varied by changing the fiber radius, flow rate, or the fluid viscosity). We show in Secs. III and IV that the composite parameters δ, η, and $\beta^{\star}$ are well suited to define the boundaries between the different regimes.

III. SOLITARY WAVES AND DYNAMICAL SYSTEMS THEORY

Experimental studies [3–6] reported the formation of axisymmetric traveling waves (TWs) propagating without deformations and at constant speed over long distances. Solitary waves, that is, TWs separated by constant-thickness layers of fluid, or substrates, much longer than the characteristic length of the waves, were commonly observed sufficiently far downstream. Theoretically, solitary waves can be viewed as periodic TWs with an infinitely long wavelength. The aim of this section is to investigate infinite-domain solitary waves using elements from dynamical systems theory.

In a frame of reference moving with the speed c of the waves, $\xi = x - ct$, the flow is stationary and the set of partial differential equations (3) can be converted into a set of ordinary differential ones. The mass balance (3a) can be integrated once,

$$q - c\left(h + \frac{\tilde{\alpha}}{2}h^2\right) \equiv q_0, \tag{12}$$

where q_0 is the rate at which the fluid flows under the waves. The averaged momentum balance (3b) next reads

$$\delta\left[cq' - F(\tilde{\alpha}h)\frac{q}{h}q' + G(\tilde{\alpha}h)\frac{q^2}{h^2}h'\right] + \frac{I(\tilde{\alpha}h)}{\phi(\tilde{\alpha})}\left[-\frac{3\phi(\tilde{\alpha})}{\phi(\tilde{\alpha}h)}\frac{q}{h^2} + h\left\{1 + h''' + \frac{\beta}{(1+\tilde{\alpha}h)^2}h' + \frac{\tilde{\alpha}}{1+\tilde{\alpha}h}h'\left[h'' - \frac{1}{2}\frac{\tilde{\alpha}}{1+\tilde{\alpha}h}(h')^2\right]\right\}\right]$$
$$+ \eta\left[J(\tilde{\alpha}h)\frac{q}{h^2}(h')^2 - K(\tilde{\alpha}h)\frac{q'h'}{h} - L(\tilde{\alpha}h)\frac{q}{h}h'' + M(\tilde{\alpha}h)q''\right] = 0, \tag{13}$$

where the primes denote differentiation with respect to the moving coordinate ξ. Using (12), (13) can be recast into $h''' = f(h, h', h'')$, where f is a function of the thickness h, its first and second derivatives, and the parameters δ, $\tilde{\alpha}$, η, and c. We thus end up with a dynamical system of dimension three,

$$\frac{d}{d\xi}\mathbf{U} = (U_2, U_3, f(U_1, U_2, U_3))^t, \tag{14}$$

where $\mathbf{U} = (U_1, U_2, U_3)^t \equiv (h, h', h'')^t$.
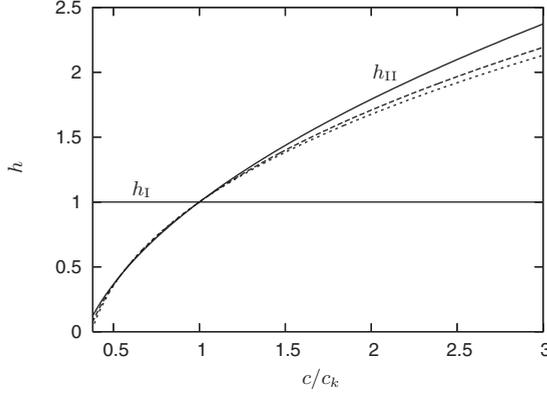
FIG. 1. Film thicknesses $h_I = 1$ and h_{II} corresponding to the location of the fixed points as function of the ratio of the normalized wave speed c to the kinematic wave speed c_k defined in Eq. (11). Solid, dashed and dotted lines refer to $\tilde{\alpha} = 0$ (planar case), $\tilde{\alpha} = 0.5$, and $\tilde{\alpha} = 1$, respectively.

Solitary waves correspond to homoclinic orbits in the phase space connecting a fixed point to itself. Here we restrict our attention to single-loop homoclinic orbits corresponding to single-hump solitary waves in real space. The fixed points of the dynamical system (14) satisfy $h' = h'' = 0$ and

$$\frac{h^3}{3} \frac{\phi(\tilde{\alpha} h)}{\phi(\tilde{\alpha})} - c\left(h + \frac{\tilde{\alpha}}{2} h^2\right) = q_0. \quad (15)$$

Requiring that $h = 1$ is a solution to (15) gives

$$q_0 = \frac{1}{3} - c\left(1 + \frac{\tilde{\alpha}}{2}\right). \quad (16)$$

In addition to the solution $h = 1$, there is one more real positive solution to (15) with (16) and the dynamical system (14) admits two fixed points $\mathbf{U}_I = (1,0,0)^t$ and $\mathbf{U}_{II} = (h_{II},0,0)^t$ whose positions are displayed in Fig. 1 as functions of the wave speed c and aspect ratio $\tilde{\alpha}$. The two fixed points coincide when the wave speed c is equal to the speed of linear waves of infinitesimal amplitude and infinite length that are neutrally stable. This situation corresponds to the definition of the linear kinematic waves in the zero-wave-number limit, whose speed is given in Eq. (11). In the limit $\tilde{\alpha} = 0$, we recover the expression $h_{II} = -1/2 + \sqrt{3(c - 1/4)}$ corresponding to a film flowing down an inclined plane [11,29]. We note that extending this expression to the axisymmetric geometry by replacing c with c/c_k, gives a reasonable approximation $h_{II} \approx -1/2 + \sqrt{3[(c/c_k) - 1/4]}$ for the position of the second fixed point even for $\tilde{\alpha} = O(1)$ (see Fig. 1). Finally, we note that it is sufficient to consider homoclinic orbits around only one of the two fixed points because of the presence of a continuous family of Nusselt flat-film solutions parameterized by the reduced Reynolds number δ (or $h_N = \bar{h}_N / l_\nu$) when Go and Γ are held constant. Indeed, homoclinic orbits connecting $\mathbf{U}_{II}$ correspond to phase-space trajectories connecting $\mathbf{U}_I$ through the transformation $h_N \rightarrow h_N h_{II}$.

The shape of the tail and front of a solitary wave can be determined by considering how the corresponding homoclinic orbit in the phase space approaches and leaves the fixed point it connects to. Let us consider the linear stability of the fixed point $\mathbf{U}_I$. The dispersion relation governing infinitesimal

perturbations $\sim \exp(\lambda \xi)$ is

$$\lambda^3 + \lambda^2 \eta D_\eta + \lambda \delta D_\delta - 3(1 + \tilde{\alpha})(c - c_k) = 0, \quad (17)$$

where

$$D_\eta = \frac{\phi}{I}\left[-\frac{L}{3} + c(1 + \tilde{\alpha})M\right], \quad (18a)$$

$$D_\delta = \left\{\frac{\phi}{I}\left[(1 + \tilde{\alpha})\left(c^2 - \frac{F}{3}c\right) + \frac{G}{9}\right] + \frac{\beta}{\delta(1 + \tilde{\alpha})^2}\right\}, \quad (18b)$$

and where the coefficients F, G, L, and M defined in Eq. (A1) are computed with the argument $m = \tilde{\alpha}$. Equation (17) can be reduced to the canonical form $P(y) = y^3 + py + q = 0$ by the change of variable $\lambda = y - \eta D_\eta / 3$, where

$$p = \delta D_\delta - \frac{\eta^2 D_\eta^2}{3}, \quad (19a)$$

$$q = -3(1 + \tilde{\alpha})(c - c_k) - \frac{\delta \eta}{3} D_\delta D_\eta + \frac{2\eta^3}{27} D_\eta^3. \quad (19b)$$

Using the Cardan formulas, (17) admits a real eigenvalue and a complex conjugate pair when the discriminant $\Delta = 4p^3 + 27q^2$ is > 0. When $\Delta < 0$, (17) admits three real eigenvalues. Therefore, $\mathbf{U}_I$ changes from a saddle to a saddle focus at $\Delta = 0$. When $\mathbf{U}_I$ is a saddle, the homoclinic orbit departs and returns to the fixed point monotonically along the two eigenspaces corresponding to the eigenvalues of smallest absolute value, and the corresponding tail and front of the solitary wave are monotonic. Conversely, when $\mathbf{U}_I$ is a saddle focus, the homoclinic orbit leaves monotonically along the eigenspace spanned by the eigenvector corresponding to the real eigenvalue and returns to the fixed point by spiraling on the eigenspace spanned by the eigenvectors corresponding to the complex pair. This spiral corresponds to capillary ripples at the front of the solitary wave while the tail remains monotonic.

Figure 2 displays the speed and maximum amplitude of the solitary waves corresponding to homoclinic orbits around $\mathbf{U}_I = (1,0,0)^t$. Parameters correspond to the fluid properties of silicon oil v50 ($\Gamma = 5.48$, see Table I) and to different fiber radii, $R = 1.5$, 0.35, and 0.25 mm (Go = 1, 0.24, and 0.17). The solutions have been computed by continuation using AUTO97 together with its subroutine HOMCONT [30]. In all cases $\Delta > 0$; that is, $\mathbf{U}_I$ is a saddle focus and the solitary waves are characterized by monotonic tails and oscillatory fronts.

Two different behaviors can be observed for small and large thicknesses, or for $\delta \ll 1$ and $\delta > 1$. For small thicknesses ($\delta \ll 1$), the maximum height h_{max} and speed of the solitary waves exhibit local maxima which strongly increase for thin fibers corresponding to a stronger RP instability. In Figs. 2(a) and 2(b), the characteristics of the solitary-wave solutions of the WRIBL model (3) and of the CM equation (5) are compared showing reasonable agreement. As the CM equation is parameterized by the aspect ratio $\tilde{\alpha}$ and β, the local maxima are the result of the balance of curvature effects and the advection by the flow. This is reminiscent of the sharp increase, or "blow-up," of speed and amplitude observed by Kalliadasis
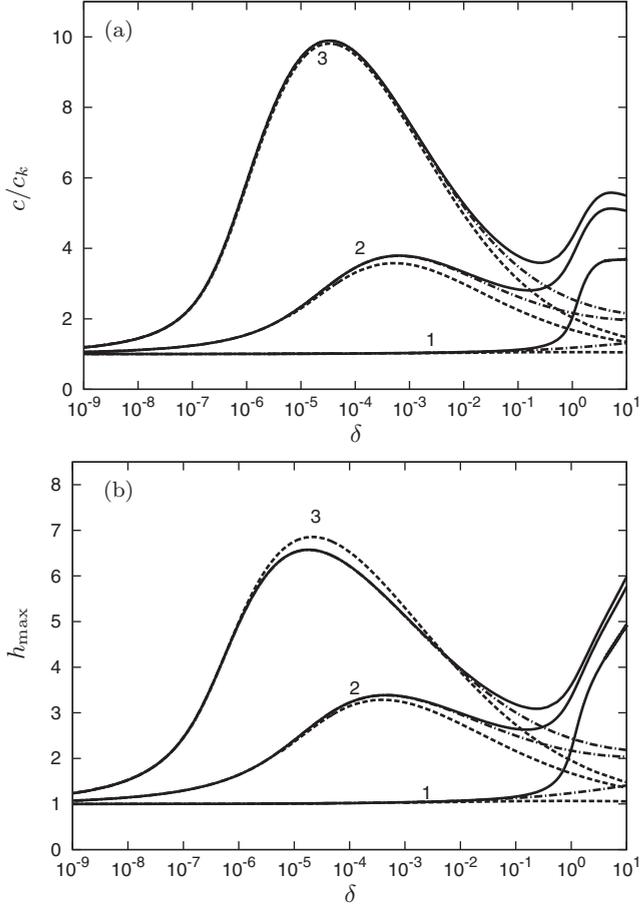
FIG. 2. Speed c (left) and maximum height h_{max} (right) of the solitary waves as function of the reduced Reynolds number δ for different fiber radii: $R = 1.5$ mm (curves 1), 0.35 mm (2), and 0.25 mm (3). Solutions to (3) (solid lines) are compared to the solutions of the CM equation (5) and of the model (3) when inertial terms are set to zero (dashed and dashed-dotted lines). The fluid properties correspond to Rhodorsil silicon oil v50 (see Table I).

and Chang [14] at $\beta = \beta_c \approx 1.413$ in their study of the solitary-wave solutions of the Frenkel equation (6).

One might expect that the sharp increase of the local maxima of the speed and amplitude observed by lowering the fiber radius is related to the nonlinear saturation mechanism of the instability by the advection discussed earlier and, therefore, it should be correlated with the saturation number $\beta^{\star}$. The validity of this hypothesis is checked in Fig. 3, where the maximum height of the solitary waves is depicted as a function of $\beta^{\star}$. At a given value of the Goucher number Go, $\beta^{\star}$ reaches a maximum for $\tilde{\alpha} \approx 0.44$ and tends to zero for $\tilde{\alpha} \to 0$ and $\tilde{\alpha} \to \infty$. For a fixed radius R, δ and $\tilde{\alpha}$ have the same trend. This explains why $\beta^{\star}$ tends to zero when $\delta \to 0$ and $\delta \to \infty$ and justifies the shapes of the curves. The local maximum of h_{max} occurs at $\beta^{\star}$ close to the maximum reached by this parameter as δ is varied. The increase of the local maximum of h_{max} is related to the increase of the maximal value of $\beta^{\star}$ achieved as the ratio Go is lowered.

We have also computed solutions of model (3) when the inertial terms are canceled ($\delta \to 0$). The results are shown as dashed-dotted lines in Figs. 2(a) and 2(b). As they asymptote to
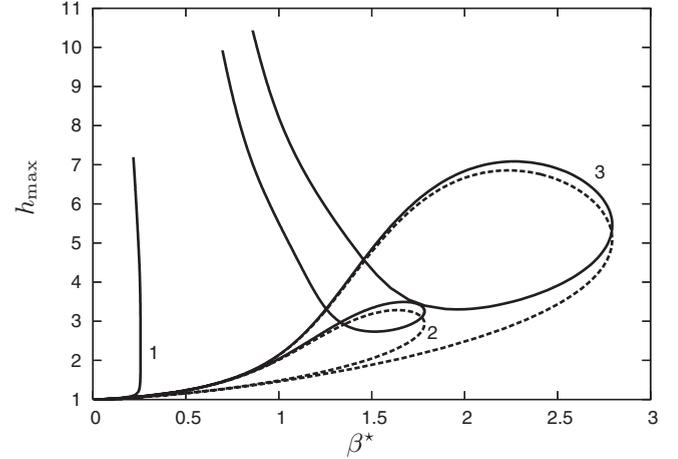
FIG. 3. Maximum height of solitary waves versus saturation parameter $\beta^{\star}$. See also caption of Fig. 2.

the solid lines corresponding to (3) in the limit $\delta \ll 1$, we can conclude that the difference in speed and amplitude between solutions to (3) and to the CM equation results from the viscous dispersion effects.

We note that for $\delta \gtrsim 10^{-2}$, viscous dispersion effects contribute to a significant increase of the speed and amplitude of the solitary waves. This unexpected nontrivial amplifying effect of viscous dispersion can be understood by considering the ratio τ_a/τ_g based on the dispersion relation corresponding to (3) in the limit $\delta \to 0$, which reads

$$\omega = k\,c_k(\tilde{\alpha}) - \eta k^2 \frac{\phi}{9(1+\tilde{\alpha})I}\left[Lk - 3(1+a)M\omega\right]$$
$$+ \frac{i\,k^2}{3(1+\tilde{\alpha})}\left(\frac{\beta}{(1+\tilde{\alpha})^2} - k^2\right). \tag{20}$$

Equation (20) corresponds to the dispersion relation obtained from the CM equation (5) augmented with a term $\propto \eta k^2$. Linear long waves ($k \ll 1$) travel at a speed which is close to c_k and the effect of second-order viscous terms on these waves can be evaluated by substituting ω with kc_k for ω in Eq. (20) except for the "critical term" $c_k k - \omega$ [18,31]. We thus get

$$\omega = k\,c_k(\tilde{\alpha}) - \eta\,\Upsilon_\eta(\tilde{\alpha})k^3 + \frac{i\,k^2}{3(1+\tilde{\alpha})}\left(\frac{\beta}{(1+\tilde{\alpha})^2} - k^2\right), \tag{21}$$

where $\Upsilon_\eta = \phi[(1+\tilde{\alpha})Mc_k - L/3]/[3(1+\tilde{\alpha})I]$ is a positive function of $\tilde{\alpha}$. The main effect of second-order viscous terms on kinematic long waves is therefore dispersive with a reduction of their waves speed from c_k to $c_k - \eta\Upsilon_\eta(\tilde{\alpha})k^2$, which thus justifies the use of the term "viscous dispersion" as already discussed in Sec. I (see also [18]).

The growth time $\tau_g = 1/\omega_i(k = k_{max})$ computed from (21) remains given by $12(1+\tilde{\alpha})^5/\beta^2$ as in Eq. (9), whereas the advection time $\tau_a = 1/\omega_r(k = k_{max})$ is converted to $\sqrt{2}(1 + \tilde{\alpha})/[c_{k,\eta}\sqrt{\beta}]$, where $c_{k,\eta} = c_k - \Upsilon_\eta(\tilde{\alpha})\beta/[2(1+\tilde{\alpha})^2]$. The ratio τ_a/τ_g thus becomes

$$\tau_a/\tau_g = \frac{\sqrt{2}}{12}(\beta^{\star})^{3/2}\frac{c_k}{c_{k,\eta}}. \tag{22}$$

Since $c_{k,\eta} < c_k$, the saturation of the instability by the flow advection is therefore attenuated by viscous dispersion which reduces the wave speed and thus raises the time τ_a of advection of the structures.

However, the maximum of the temporal growth rate given by (21) is reached at $k = k_{RP}/\sqrt{2}$, which in practice is not small. The previous argument is therefore not strictly valid in this case. The advection time τ_a and the typical growth time τ_g corresponding to (20) are complicated functions of $\tilde{\alpha}$ and Go. Viscous dispersion decelerates the wave and increases τ_a, but also damps the RP instability and thus simultaneously raises τ_g. Yet, τ_a increases more rapidly than τ_g as η is raised. The deceleration of the waves by viscous dispersion is thus more significant than its damping effect. The waves have therefore more time to grow before reaching saturation, which explains their nontrivial amplification by viscous effects.

Figure 2 reveals a sharp increase of the maximum height and speed of the waves above $\delta \approx 2$, corresponding to the predominance of the K mode. The characteristics of the waves in this region will be considered in detail later on in Sec. IV B. Let us simply stress here that the increase of the wave amplitude is also accompanied by a sharp increase of the maximum gradient of the film height, $\max |h'|$. The separation between the local maxima for the speed and amplitude corresponding to the RP-dominated waves ($\delta \ll 1$) and the K-dominated waves at large δ increases for even more viscous fluids like the castor oil used by Kliakhandler [3] (cf. Table I), as can be observed when Fig. 2 is redrawn for $\Gamma = 0.45$ (not shown). This increase can be understood by considering the definition of $\beta^\star$, which is a function of the aspect ratio $\tilde{\alpha}$ and Go and the definition of $\delta = (\tilde{\alpha}Go)^{11/3}\phi(\tilde{\alpha})\Gamma^{3/2}$. Since Γ decreases with the kinematic viscosity, the maximum of $\beta^\star$ for a given value of Go corresponds to smaller and smaller values of δ as the viscosity of the fluid is increased. In contrast with the results for silicon oil v50 (cf. Fig. 2), a transition from a saddle focus to a saddle fixed point has been observed corresponding to the disappearance of the capillary ripples at the front of the solitary wave at values of δ above 0.1.

Conversely, the separation of the solitary-wave characteristics, such as speed and maximum height, as a function of δ into two distinct regions, at low and high reduced Reynolds numbers, vanishes at low viscosities. Indeed, at low viscosities, or equivalently, high Kapitza numbers, the RP mode occurs at relatively high values of δ, where the K mode already takes over. In Fig. 4(a) we have redrawn Fig. 2(b) for water ($\Gamma = 3376$; see Table I), which is 50 times less viscous than silicon oil v50. The figure compares the maximum height of the solitary waves for a ratio of the Goucher number Go equal to the ones chosen for the computations shown in Figs. 2, to the amplitude of the solutions of the CM equation (5). At small values of δ, the amplitude of the waves is significantly larger than the amplitude of the solutions of the CM equation, which signals the influence of the K mode on the RP instability. Notice that this effect cannot arise from the second-order viscous terms as the cancellation of the inertial terms leads to results comparable to the solutions of the CM equation. On the other hand, the influence of the RP instability on the K mode is illustrated in Fig. 4(b), where $\beta^\star$ and $h_{\max}$ are plotted versus δ. At small fiber radii $R = 0.64$ mm and $R = 0.46$ mm (Go = 0.24 and 0.17), the characteristic sharp increase of the
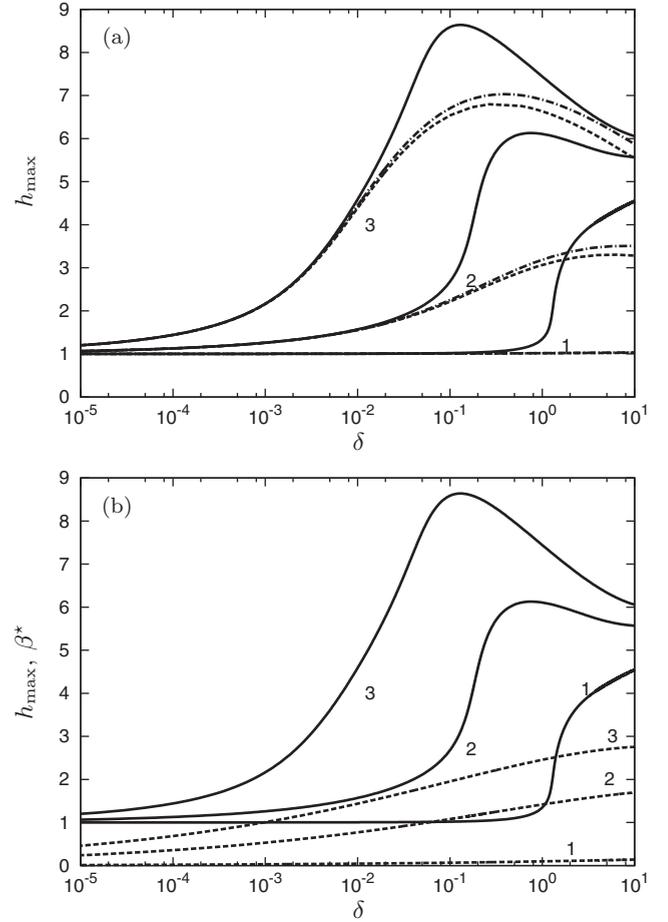
FIG. 4. (a) Maximum height $h_{\max}$ of the solitary waves as a function of δ. Solutions of (3) (solid lines) are compared to the solutions of the CM equation (5) (dashed lines) and solutions of (3) where the inertia terms are set to zero (dashed-dotted lines). (b) Maximum height $h_{\max}$ (solid line) and parameter $\beta^\star$ (dashed lines). Parameters correspond to water ($\Gamma = 3376$) and different fiber radii: $R = 2.75$ mm (curves 1), 0.64 mm (2), and 0.46 mm (3).

solitary-wave amplitude is displaced to values of δ smaller than $\delta \approx 2$ corresponding to a generalized saturation number $\beta^\star \gtrsim 1$.

IV. LIMITING CASES

In this section, we focus on the different regions of the wave-characteristics' diagrams displayed in Figs. 2 and 4 and consider all possible asymptotic limits.

A. Small Goucher number limit: The droplike regime

Let us first consider the local maxima of the amplitude $h_{\max}$ and speed c with respect to δ for given values of the Goucher number Go, or equivalently $\tilde{\alpha}$, observed for viscous fluids like silicon oils in the inertialess limit ($\delta \ll 1$). From Fig. 2, it is clear that the CM equation and the WRIBL model give very close results since the former is recovered from the latter as δ and η are set to zero. Since only $\tilde{\alpha}$ and $\beta = \tilde{\alpha}^{2/3}Go^{-4/3}$ enter in the CM equation (5), the local maxima of $h_{\max}$ and speed c are functions of $\tilde{\alpha}$ and Go only (and thus do not

TABLE III. Local maxima of the speed c and amplitude h_{max} with respect to δ for given values of the Goucher number Go, or equivalently $\tilde{\alpha}$, obtained from the CM equation (5). c_{drops} refers to the speed of quasistatic drops sliding down coated fibers (see text and Appendix B).

Go	$\tilde{\alpha}$	h_{max}	c	$\bar{h}_{max}/\bar{R}$	$c\,\nu/(g\bar{R}^2)$	$c_{drops}\,\nu/(g\bar{R}^2)$
0.236	0.23	3.3	3.1	0.77	0.22	0.25
0.168	0.15	6.9	8.8	1.05	0.25	0.30
0.110	0.075	18	38.5	1.36	0.24	0.29
0.055	0.022	81.2	383	1.80	0.19	0.22
0.044	0.014	129	773	1.85	0.16	0.18

depend on Γ). Table III depicts these quantities as obtained from the CM equation. As Go tends to zero, the RP instability mechanism becomes more and more efficient and we observe a sharp increase of the local maxima of the amplitude h_{max} and of the maxima of the speed of the waves. For such waves, the amplitude can be several orders of magnitude larger than the Nusselt flat film on which they stand, and variations of the Nusselt thickness should only slightly modify the wave characteristics (except perhaps when the film becomes so thin that the corner dissipation at the wave front dominates over the dissipation in the bulk).

Since $\bar{R} \ll l_c$, azimuthal surface tension effects dominate over gravity and the typical length scale and height of a wave should correspond to the radius $\bar{R}$ of the fiber as already pointed out in Sec. II B. The wave speed should then be determined by the balance of viscosity and gravity at the scale $\bar{R}$, which gives a typical velocity of $g\bar{R}^2/\nu$ for viscous-gravitational drainage. Justification of the neglect of the inertial terms demands that the Galilei number Ga $=$ Go$^3\Gamma^{3/2}$ is small, which is satisfied for all tested fluids except for water ($\Gamma = 3376$). Our computations of the solutions to the CM equation (5) confirm these scaling arguments as shown in Table III.

In Fig. 5, we contrast the wave profiles rescaled with respect to $\bar{R}$ corresponding to Table III. Except from the front and back of the waves corresponding to the return to the fixed point, the wave profiles are rather symmetric. This front-to-

back symmetry shows that gravity does not affect the wave profile, as expected, since the typical size of the wave $\bar{R}$ is much smaller than the capillary length l_c. Therefore, solitary waves in this regime resemble isolated drops sliding under the action of gravity on a wettable fiber, which is precisely why we refer to this regime as the droplike regime. [When $\bar{R}$ is larger and approaches l_c, on the other hand, the drops will feel the effect of gravity as they grow and they will eventually resemble falling pendant drops.] It corresponds to the observation by Quéré [2,26] in the coating of wires or thin fibers drawn out of a bath of viscous liquids that the thin annular film deposited on the wires and fibers breaks up into drops.

We have checked this analogy by computing the shape of static drops with zero contact angles sitting on a fiber coated with a base liquid film, or substrate film, of the same liquid (details of the calculation are given in Appendix B). The agreement of the wave shapes to the symmetrical static drop shapes is remarkable even in the case of nearly spherical drops such as those obtained at Go $= 0.044$, where the long-wave assumption is no longer valid. We can therefore conclude that the CM equation (5), and by extension the WRIBL model (3), are accurate in the droplike regime where surface tension is dominant and even if the long-wave approximation does not hold. Besides, the remarkable agreement between the solutions to the CM equation (5) and the WRIBL model (3) already noted in Fig. 2, shows that the second-order streamwise viscous terms do not affect the amplitude and speed of the drops.
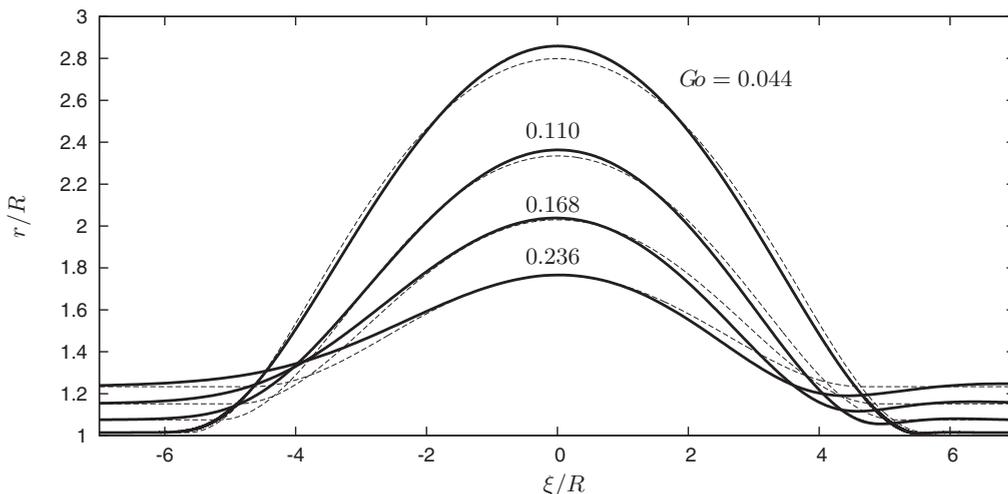
FIG. 5. Wave profiles corresponding to the solutions to the CM equation (solid lines) and static drop shape (thin dashed lines). Labels correspond to the Goucher number. Values of the other parameters are listed in Table III.
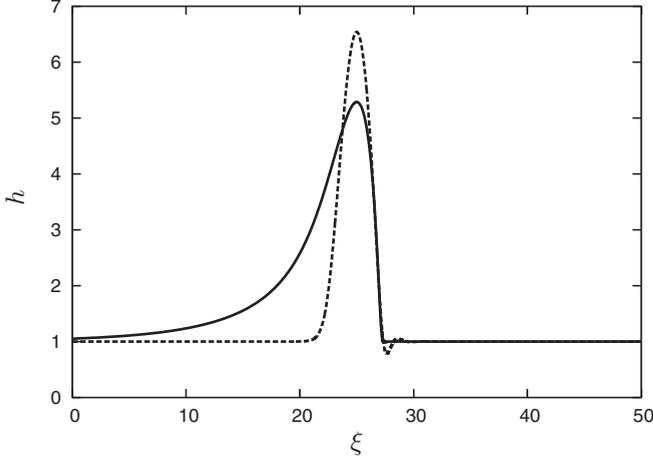
FIG. 6. Profile of single-loop homoclinic solutions to (3) corresponding to single-hump solitary waves. Parameters correspond to Rhodorsil silicon oil v50 ($\Gamma = 5.48$) and $R = 0.25$ mm. Solid and dashed lines refer to $\delta = 5$ and $\delta = 3 \times 10^{-5}$, respectively.

Following [14], an analytical estimate of the amplitude and speed of the droplike waves in the limit Go $\rightarrow$ 0 may be obtained via matched asymptotic expansions. The appropriate small parameter is the dimensionless speed of the drops. By balancing viscous and capillary forces at the back of the waves, one can easily extend to sliding drops the Landau-Levich-Derjaguin law obtained by Quéré [26] in the case of fibers drawn out of a bath. The speed of sliding drops is thus governed by Eq. (B4), which compares favorably to the results from the CM equation in Table III. As a matter of fact, this agreement shows that the thickness of the residual film on which the drops slide is determined by the balance of surface tension and viscous dissipation in the meniscus region. To estimate the speed and amplitude of droplike waves, one would have to take into account the gravity acceleration and higher-order corrections in the outer region, namely the viscous dissipation in the drop, a task which is difficult, as (a) with the Frenkel equation resolving fully the leading-order outer region requires matching up to third order [14] and quite likely this is the case here, (b) a single "composite equation" for the whole domain, that is, for both the drop and residuals films, as, for example, in the "drag-out" problem in coating theory [32], does not exist.

B. Large δ limit: The drag-inertia regime

Even though, strictly speaking, δ is not allowed to tend to infinity within the long-wave approach, the question of the behavior of the different quantities of interest for large δ is a valid one within the context of the WRIBL model as model equations. Besides the change of behavior of the speed and amplitude of the waves that occur around $\delta \approx 1$ will be clarified by the asymptotical analysis.

To understand the change of behavior of the solitary-wave characteristics at relatively large values of δ, it is instructive to look at the wave profiles. Figure 6 compares two single-loop homoclinic orbits for a small and a large value of δ. For $\delta \ll 1$, solitary waves have a relatively symmetric shape. Except from

the neighborhood of the fixed point $\mathbf{U}_\mathrm{I}$, where the escape from $\mathbf{U}_\mathrm{I}$ is monotonic and the return to it is oscillatory, a symmetry between the front and the back of the waves is observed with a steep front and a steep back. On the contrary, at large values of δ, the front and back of the solitary waves present radically different shapes, with a gentle sloping back edge and a steep front edge.

The observed difference between the front and the back of the solitary waves in the large-δ case can be explained by examining the linearized dynamics around $\mathbf{U}_\mathrm{I}$. The dispersion relation governing infinitesimal perturbations varying as $\exp(\lambda\xi)$ is given in Eq. (17). At a given radius R and capillary length l_c, large thickness, $h_\mathrm{N} \gg 1$, corresponds to $\delta \sim h_\mathrm{N}^{11/3}\phi(\tilde{\alpha}) \gg 1$, $\beta/\delta = (l_c/R)^2/(3\mathrm{Re}) \ll 1$ and possibly large viscous dispersion since $\eta \sim h_\mathrm{N}^{4/3}$. Let λ_1 be the positive eigenvalue corresponding to the unstable manifold of $\mathbf{U}_\mathrm{I}$. The eigenvalues of the tangent subspace to the unstable manifold satisfy $\mathrm{Re}(\lambda_3) \leqslant \mathrm{Re}(\lambda_2) < 0$. When $\mathbf{U}_\mathrm{I}$ is a saddle focus ($\Delta > 0$), we further denote $\lambda_{2,3}$ by $-\Sigma \pm i\Omega$ with $\Sigma > 0$ and $\Omega > 0$. From (17) we obtain the estimate $\lambda_1 \sim \delta^{-1} \ll 1$. Since $\lambda_1 + \lambda_2 + \lambda_3 = -\eta D_\eta$, we immediately get an estimate of the mean value, $(\lambda_2 + \lambda_3)/2 \sim -\eta$, so that $\Sigma \sim \eta$ when $\Delta > 0$. As a consequence, at the back of a solitary wave, the monotonic escape from the fixed point is slow, whereas at the front, the return to $\mathbf{U}_\mathrm{I}$ is fast. The above estimates have been confirmed by computations of λ_1 and Σ for the solitary waves shown in Fig. 2 corresponding to silicon oil v50. A direct consequence is that for $\delta \gg 1$ the long-wave assumption does not hold at the fronts of the waves, whereas it is still verified at their backs: the WRIBL model cannot accurately capture the front regions—the "capillary shocks"—but still adequately describe the backs of the waves and thus their amplitude and speed [11].

Focusing now at the back of the solitary wave and defining a slow variable $\tilde{\xi} = \xi/\delta$, (13) reads

$$\left\{ (1 + \tilde{\alpha}h)\left[c^2 - cF(\tilde{\alpha}h)\frac{q}{h} \right] + G(\tilde{\alpha}h)\frac{q^2}{h^2} \right. $$
$$\left. + \frac{\beta I(\tilde{\alpha}h)}{\delta(1 + \tilde{\alpha}h)^2\phi(\tilde{\alpha})} \right\} \frac{\mathrm{d}h}{\mathrm{d}\tilde{\xi}} \frac{I(\tilde{\alpha}h)}{\phi(\tilde{\alpha})} \left[\frac{3\phi(\tilde{\alpha})}{\phi(\tilde{\alpha}h)}\frac{q}{h^2} - h \right] $$
$$+ O(\eta/\delta^2, \delta^{-3}), \tag{23}$$

where q is given by (12) and (16). Equation (23) can be formally rewritten as

$$\mathcal{G}(h,c;\tilde{\alpha},\beta/\delta)\frac{\mathrm{d}h}{\mathrm{d}\tilde{\xi}} = -\mathcal{H}(h,c;\tilde{\alpha}) + O(\eta/\delta^2, \delta^{-3}), \tag{24}$$

expressing the balance at the back of the solitary waves of inertia (at the left-hand side), viscous drag, and gravity acceleration (at the right-hand side). As a consequence, the roots of the right-hand side of (23) correspond to the fixed points of (14).

As the homoclinic orbit departs from $\mathbf{U}_\mathrm{I}$, h increases up to h_II, which is larger than unity since $c > c_k$ (cf. Fig. 1). At this point, h goes through a maximum if $\mathcal{G}$ is nonzero. The resulting orbit is thus a heteroclinic one linking $\mathbf{U}_\mathrm{I}$ and $\mathbf{U}_\mathrm{II}$ which contradicts the fact that we are considering a single-loop homoclinic orbit [11]. As a consequence, $\mathcal{G}$ must go to zero at $h = h_\mathrm{II}$, which signals a "critical film thickness" h_c at which

inertial terms must go to zero. In the limit $\delta \to \infty$, we thus obtain the condition

$$h_{\mathrm{II}}(c;\tilde{\alpha}) = h_c(c;\tilde{\alpha},\beta/\delta), \qquad (25)$$

which gives a unique solution c_{crit} and then h_{crit} as function of $\tilde{\alpha}$ and β/δ. As the limit speed c_{crit} is governed by the balance of inertia, wall friction, and gravity acceleration, we may refer to this situation as the *drag-inertia* regime [10].

Having shown that $\mathcal{G}$ possesses at least one root, $\mathcal{G}$ can be factorized into $\mathcal{G} = (1 + \tilde{\alpha}h)[c - c_{d+}(\tilde{\alpha}h,q/h,\beta/\delta)][c - c_{d-}(\tilde{\alpha}h,q/h,\beta/\delta)]$, where

$$c_{d\pm}(\tilde{\alpha}h,q/h) = \frac{q}{h}\frac{F(\tilde{\alpha}h)}{2} \pm \sqrt{\Delta_{\tilde{\alpha}h,q/h,\beta/\delta}} \qquad (26a)$$

and

$$\Delta_{\tilde{\alpha}h,q/h,\beta/\delta} = \left(\frac{q}{h}\right)^2 \left[\frac{F(\tilde{\alpha}h)^2}{4} - \frac{G(\tilde{\alpha}h)}{1+\tilde{\alpha}h}\right] \\ - \frac{\beta I(\tilde{\alpha}h)}{\delta(1+\tilde{\alpha}h)^3\phi(\tilde{\alpha})} \qquad (26b)$$

are the speeds of linear dynamic waves for a uniform layer of thickness h and averaged speed q/h [18]. In other words, the position of the second fixed point must coincide with the critical layer h_c at which the speed of the solitary wave c is equal to the speed of one of the dynamic waves $c_{d\pm}$—in fact the fastest one with speed c_{d+}—which separates the flow into a "subcritical region" ($c < c_{d+}$) and a "supercritical region" ($c > c_{d+}$). The condition $h_{\mathrm{II}} = h_{\mathrm{crit}}$ is similar to the "Thomas condition" derived in the mathematical treatment of periodic bores on steep slopes, or *roll waves* [33,34] made of the regular succession of laminar flows and hydraulic jumps. For $\delta \gg 1$, the front of the solitary waves, where surface tension arrests the breaking of the waves, plays a role similar to that of a hydraulic jump connecting the subcritical and supercritical regions of a roll wave. For this reason, we may also refer to this regime as the *roll-wave regime*.

Considering now large but finite values of δ, condition (25) is not verified and one has to go back to (24). At the critical point $h = h_c$ we have $\mathcal{G}(h_c,c;\tilde{\alpha}) = 0$ and a Taylor expansion close to criticality gives

$$h_c - h_{\mathrm{crit}} \approx -[\partial_c \mathcal{G}/\partial_h \mathcal{G}](h_{\mathrm{crit}},c_{\mathrm{crit}})(c - c_{\mathrm{crit}}) \qquad (27)$$

whenever $\partial_h \mathcal{G}(h_{\mathrm{crit}},c_{\mathrm{crit}}) \neq 0$. Proceeding next to a Taylor expansion of $\mathcal{H}(h,c)$, (24) yields

$$\left[\partial_c \mathcal{H} - \frac{\partial_h \mathcal{H} \partial_c \mathcal{G}}{\partial_h \mathcal{G}}\right](c - c_{\mathrm{crit}}) \approx K_\eta \frac{\eta}{\delta^2} + \frac{K_{\mathrm{st}}}{\delta^3}, \qquad (28)$$

where the constants K_η and K_{st} are functions of h_{crit}, c_{crit} and the derivatives h'_{crit}, h''_{crit} and at h'''_{crit} at the critical thickness of the asymptotic solution. Since for $h_{\mathrm{N}} \gg 1$, $\delta \sim h_{\mathrm{N}}^{11/3}$ and $\eta \sim h_{\mathrm{N}}^{4/3}$ the asymptotically dominant terms in the right-hand side of (28) are the viscous terms $K_\eta \eta \delta^{-2}$. Consequently, the convergence of the speed of the waves to the asymptotic value $c_{\mathrm{crit}}(\tilde{\alpha})$ satisfies

$$c - c_{\mathrm{crit}}(\tilde{\alpha},\beta/\delta) \propto \eta/\delta^2 \sim 1/\mathrm{Re}^2, \qquad (29)$$

in agreement with our numerical computations.

Figure 7 compares the phase speed c of the solitary waves to the asymptotic limit c_{crit} as a function of δ for the four different fluids of increasing viscosity that we considered (fluid properties are gathered in Table III). For weakly viscous flows, the RP and K mode reinforce each other and the speed c of the waves is much higher than the asymptote c_{crit} [see Fig. 7(a)].

At larger viscosities [Figs. 7(b) and 7(c)] the K mode ceases to be affected by the RP instability and a rapid convergence to c_{crit} is observed as δ is increased. Whereas for very viscous fluids like silicon oil v1000 (1000 times more viscous than water; cf. Table I), the curves start again to separate, signaling the arrest of the convergence to the asymptote c_{crit} by the axial viscous effects.

C. Weakly nonlinear analysis

Let us now consider the regions of the speed and maximum height diagrams in Figs. 2 and 4 corresponding to the transition between the droplike regime and the drag-inertia regime. They correspond to situations where neither the K nor the RP instability mechanisms are strong enough to promote large amplitude waves, that is, when $\delta \lesssim 1$ and $\beta^\star \lesssim 1$. We can then proceed to a weakly nonlinear analysis to characterize the shape, speed, and amplitude of the waves. Since $\delta \ll 1$, we substitute $h = 1 + H$ and $q = 1/3 + Q$ where $H = O(\theta)$ and $Q = O(\theta)$ are small deviations from the base state $(h,q) = (1,1/3)$, (i.e., $\theta \ll 1$). Taking the distinguished limit $\theta \ll \epsilon^2$, we are led from the WRIBL (3) model to a single-evolution equation for the deviation H:

$$\partial_t H + c_k \partial_x H + \Phi(\tilde{\alpha})H\partial_x H + \frac{\beta}{3(1+\tilde{\alpha})^3}\partial_{xx}H + \frac{1}{3(1+\tilde{\alpha})}\partial_{xxxx}H$$
$$+ \delta\frac{\phi(\tilde{\alpha})}{3I(\tilde{\alpha})}\left[\partial_{tt}H + \frac{F(\tilde{\alpha})}{3}\partial_{tx}H + \frac{G(\tilde{\alpha})}{9(1+\tilde{\alpha})}\partial_{xx}H\right] + \eta\frac{\phi(\tilde{\alpha})}{3I(\tilde{\alpha})}\left[M(\tilde{\alpha})\partial_{xxt}H - \frac{L(\tilde{\alpha})}{3(1+\tilde{\alpha})}\partial_{xxx}H\right] = O(\theta\epsilon^5, \theta^2\epsilon^2), \quad (30)$$

where

$$\Phi(\tilde{\alpha}) = \frac{3(2+\tilde{\alpha})\phi + \tilde{\alpha}[(6+5\tilde{\alpha})\phi' + \tilde{\alpha}(1+\tilde{\alpha})\phi'']}{3(1+\tilde{\alpha})^2\phi} \qquad (31)$$

is a function of the aspect ratio $\tilde{\alpha}$. Noteworthy is that a stability analysis of the base state $(h,q) = (1,1/3)$ based on (30) leads to the same dispersion relation as for (3).
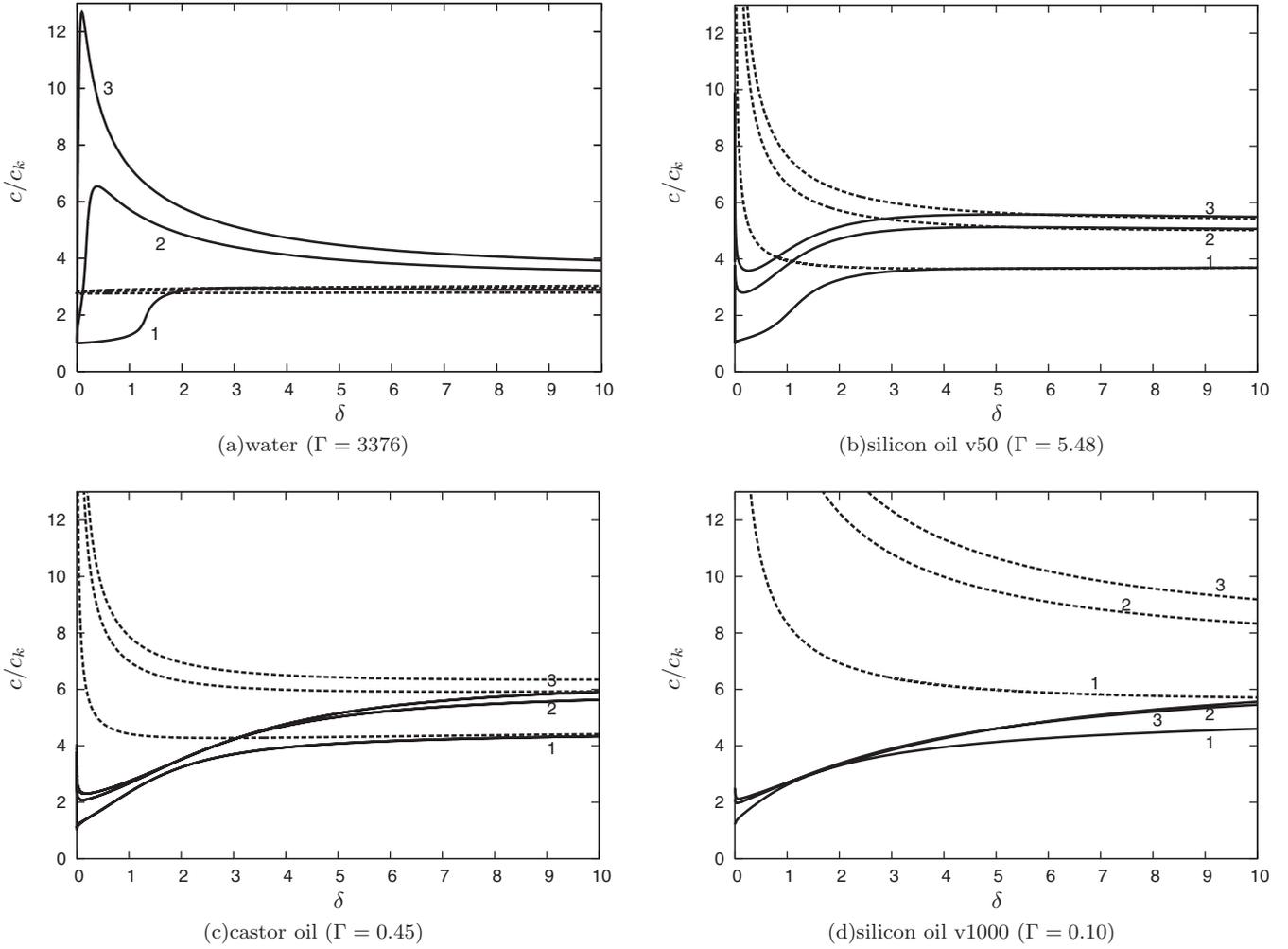
FIG. 7. Speed c of the solitary waves as a function of the reduced Reynolds number δ for three values of the Goucher number Go = 1.01 (curves 1), 0.236 (curves 2), and 0.168 (curves 3) for fluids of decreasing Kapitza numbers. Solutions to (3) (solid lines) are compared to the asymptotic predictions c_{crit} (dashed lines).

1. Drag-gravity regime

We consider here the limit of a thin film compared to the fiber radius, $\tilde{\alpha} \ll 1$, when the radius of the fiber is constant or equivalently Go is constant. Since $\eta = (\bar{h}_{\mathrm{N}}/l_c)^{4/3} = \tilde{\alpha}^{4/3}\mathrm{Go}^{4/3}$, viscous dispersion is negligible in this limit and (30) reduces to

$$\partial_t H + \partial_x H + 2H\partial_x H + \frac{\beta}{3}\partial_{xx}H$$
$$+ \frac{2}{5}\delta\left[\partial_{tt}H + \frac{17}{21}\partial_{tx}H + \frac{1}{7}\partial_{xx}H\right] + \frac{1}{3}\partial_{xxxx}H = 0. \quad (32)$$

By making use of the first-order equivalence of the time and space derivatives of H, $\partial_t H \approx -\partial_x H$, (32) reduces to the Kuramoto-Sivashinsky (KS) equation:

$$\partial_t H + \partial_x H + 2H\partial_x H + \frac{1}{3}\left[\frac{2}{5}\delta + \beta\right]\partial_{xx}H + \frac{1}{3}\partial_{xxxx}H = 0. \quad (33)$$

To look for the TW solutions to (33) in their moving frame, $\xi = x - ct$, we rescale the velocity as $c = 1 + C$ and the amplitude

as $H = \theta A$ and stretch the moving coordinate as $\xi = BX$:

$$-3CB^3 A + 3\theta B^3 A^2 + B^2\Upsilon\frac{d}{dX}A + \frac{d^3}{dX^3}A = 0, \quad (34)$$

where $\Upsilon = \frac{2}{5}\delta + \beta$ and the condition $\lim_{\xi\to\pm\infty}H = 0$ has been enforced, yielding a vanishing integration constant. Balancing each term in Eq. (34) gives $CB^3 \sim \theta B^3 \sim B^2\Upsilon \sim 1$ so that $B \sim \Upsilon^{-1/2}$, $\theta \sim \Upsilon^{3/2}$, and $C \sim \Upsilon^{3/2}$.

Writing $B = \Upsilon^{-1/2}$, $\theta = \frac{2}{3}\Upsilon^{3/2}$, and $C = \mu\Upsilon^{3/2}/3$ then leads to

$$-\mu A + 2A^2 + \frac{d}{dX}A + \frac{d^3}{dX^3}A = 0, \quad (35)$$

which is an ordinary-differential equation governing the TW solutions to the KS equation propagating at speed μ. Equation (35) admits a one-hump solitary-wave solution for a particular value of $\mu = \mu_0 \approx 1.216$ and an amplitude $A_{\max} \approx 0.784$. Consequently, in the limit $\tilde{\alpha} \to 0$, the speed c and the amplitude $h_{\max}$ of the one-hump solutions to (3) follow power laws of the form

$$c \approx 1 + 0.405\,\Upsilon^{3/2}, \quad h_{\max} \approx 1 + 0.523\,\Upsilon^{3/2}. \quad (36)$$

Recall that the relations (36) have been obtained under the assumption of small amplitude, $h_{\max} - 1 \ll 1$; hence, Υ must be small, which implies that both inertia and azimuthal curvature effects must be small. Viscous drag and gravity acceleration are the dominant physical effects. Following [10], we may refer to this regime as the *drag-gravity regime.*

It is possible to interpret this regime as one characterized by the arrest of the instability growth by the flow advection. The dispersion relation corresponding to the KS equation (33) and governing infinitesimal perturbations around the base Nusselt flow of wave number k and angular frequency ω is identical to (7) when β is substituted with Υ. One can then follow the same line of reasoning in going from (7) to (8) and define the ratio of the typical time of advection of the structure over its length, $\tau_a = k^{-1}$, to the typical time of growth, $\tau_g = [\max(\omega_i)]^{-1}$, of the instability:

$$\tau_a / \tau_g = \omega_i / \omega_r |_{k=\sqrt{\Upsilon/2}} \propto \Upsilon^{3/2}. \quad (37)$$

Therefore, $\Upsilon \ll 1$ corresponds to $\tau_a \ll \tau_g$. The flow advection is much faster than the instability and the ratio τ_a / τ_g controls the amplitude and speed of the observed structures as reflected by (36).

2. Solitonlike regime

We consider in this section the limit of a thick film, $\tilde{\alpha} \gg 1$ (though in practice, if $\tilde{\alpha}$ is large, the axisymmetry of the flow might be difficult to attain). We thus have $\phi(\tilde{\alpha}) \sim (3/4)\tilde{\alpha} \log(\tilde{\alpha})$, $c_k \sim 4/3\tilde{\alpha}^{-1}$ and $\beta^\star \sim (3/4)^{2/3} (\tilde{\alpha} \mathrm{Go})^{-4/3}$, $\delta \sim \frac{3}{4} \tilde{\alpha} \log(\tilde{\alpha}) \Gamma^{3/2} (\tilde{\alpha} \mathrm{Go})^{11/3}$, while in all cases $\eta = (\tilde{\alpha} \mathrm{Go})^{4/3}$. Therefore, the conditions $\delta \ll 1$ and $\beta^\star \lesssim 1$, necessary for the weakly nonlinear analysis, can be justified if, for example, $\tilde{\alpha}\mathrm{Go} = O(1)$, that is, $\eta = O(1)$ and $\Gamma^{3/2} \ll 1$. For silicon oil v1000, $\Gamma = 0.1$ so that $\Gamma^{3/2} = 0.03$. [We note that, strictly speaking, the derivation of the WRIBL model (3) demands that Γ is at least $O(1)$ since the long-wave approximation is sustained only when surface tension effects are strong [18].]

Neglecting inertial effects and looking for the dominant terms in Eq. (30) leads to

$$\partial_t H + \frac{4}{3\tilde{\alpha}} \partial_x H + \frac{8}{3\tilde{\alpha}} H \partial_x H + \frac{1}{3\tilde{\alpha}\eta} \partial_{xx} H$$
$$+ \frac{1}{3\tilde{\alpha}} \partial_{xxxx} H - \eta \log(\tilde{\alpha}) \left[\frac{3}{2} \partial_{xxt} H + \frac{1}{\tilde{\alpha}} \partial_{xxx} H \right] = 0. \quad (38)$$

The first-order equivalence of the time and space derivatives of H, that is, $\partial_t H = -[4/(3\tilde{\alpha})\partial_x H] + O(\epsilon\theta^2, \epsilon^2\theta)$, can again be utilized. Equation (38) is then simplified into

$$\partial_t H + \frac{4}{3\tilde{\alpha}} \partial_x H + \frac{8}{3\tilde{\alpha}} H \partial_x H + \frac{1}{3\tilde{\alpha}\eta} \partial_{xx} H$$
$$+ \frac{\eta \log(\tilde{\alpha})}{\tilde{\alpha}} \partial_{xxx} H + \frac{1}{3\tilde{\alpha}} \partial_{xxxx} H = 0, \quad (39)$$

the "Kawahara" equation that was scrutinized numerically by Kawahara and co-workers [35,36]. The equation is also often referred to as the "generalized KS" equation [21,37,38], and it is the KS equation appropriately extended to include dispersion ($\partial_{xxx} H$). As before, we look for TW solutions in their moving frame, $\xi = x - ct$. Stretching the moving coordinate as $\xi = \sqrt{\eta} X$, the amplitude as $H = \eta^{-3/2} A/2$, and the speed as

$c = (4/3)\tilde{\alpha}^{-1}(1 + \mu \eta^{-3/2}/4)$ then gives

$$-\mu A + 2A^2 + \frac{d}{dX}A + \delta_K \frac{d^2}{dX^2}A + \frac{d^3}{dX^3}A = 0, \quad (40)$$

where $\delta_K = 3\eta^{3/2} \log(\tilde{\alpha})$ is a parameter that measures the relative importance of dispersion. Equation (40) governs TW solutions of the Kawahara equation propagating at speed μ. Since $\tilde{\alpha} \gg 1$ and $\eta = O(1)$, the dispersion parameter δ_K is large, in which case the speed of the one-hump solitary-wave solutions to (40) is given by $\mu \approx 0.3256 \delta_K$. Solitary-wave solutions of (3) in the limit $\tilde{\alpha} \gg 1$ and $\delta \ll 1$ should therefore satisfy

$$\frac{c}{c_k} \approx 1 + 0.24 \log(\tilde{\alpha}). \quad (41)$$

However, our computations show that for moderate values of $\tilde{\alpha}$ the wave speed is, in fact, closer to $c/c_k \approx 1.65 + 0.24 \log(\tilde{\alpha})$. The reason for this discrepancy can be traced in the violation of the assumption of small-amplitude deviations from the base state ($h - 1 \ll 1$) that was necessary to obtain (39) from (3). Indeed, TW solutions to the Kawahara equation have a speed and an amplitude that diverge as δ_K becomes large.

D. Speed to amplitude relation

The weakly nonlinear analysis presented in Sec. IV C provides us with the dependencies (36) of the speed and maximum height as functions of $\Upsilon = \frac{2}{5}\delta + \beta$ for small film thicknesses. Combining these two relations gives a linear dependence of the deviation amplitude $h_{\max} - 1$ to the deviation speed $c/c_k - 1$, where the wave speed c has been normalized with the kinematic wave speed c_k:

$$h_{\max} - 1 \approx 1.29 \left(\frac{c}{c_k} - 1 \right). \quad (42)$$

A linear dependence of the speed as a function of amplitude was initially found by Chang [39],

$$h_{\max} - 1 \approx \frac{c}{c_k} - 1, \quad (43)$$

by utilizing a normal form analysis of the TW solutions of the KS equation (33). This linear dependence is a characteristic of the drag-gravity regime and must be contrasted with the experimental relation

$$h_{\max} - 1 \approx 1.67 \left(\frac{c}{c_k} - 1 \right) \quad (44)$$

obtained by Tihon *et al.* [40] for solitary waves running down a plane inclined at an angle $5°$. A linear dependence of $h_{\max}$ with respect to c/c_k has also been found experimentally in the recent study by [6] for solitary waves on a relatively thick fiber.

Similarly, in the droplike regime, a law relating c and $h_{\max}$ can easily be obtained by recognizing that the wave amplitude $h_{\max} - 1$ should be proportional to the distance $h_{\mathrm{II}} - 1$ separating the fixed points. The constant of proportionality is determined by continuity with (42) in the limit $h_{\mathrm{II}} - 1 \ll 1$ for which $h_{\mathrm{II}} - 1 \approx c/c_k - 1$ (see Fig. 1). Next, by approximating h_{II} with $-1/2 + \sqrt{3[c/c_k - 1/4]}$ we arrive at

$$h_{\max} - 1 \approx 1.29 \left(-\frac{3}{2} + \sqrt{3 \left[\frac{c}{c_k} - \frac{1}{4} \right]} \right). \quad (45)$$
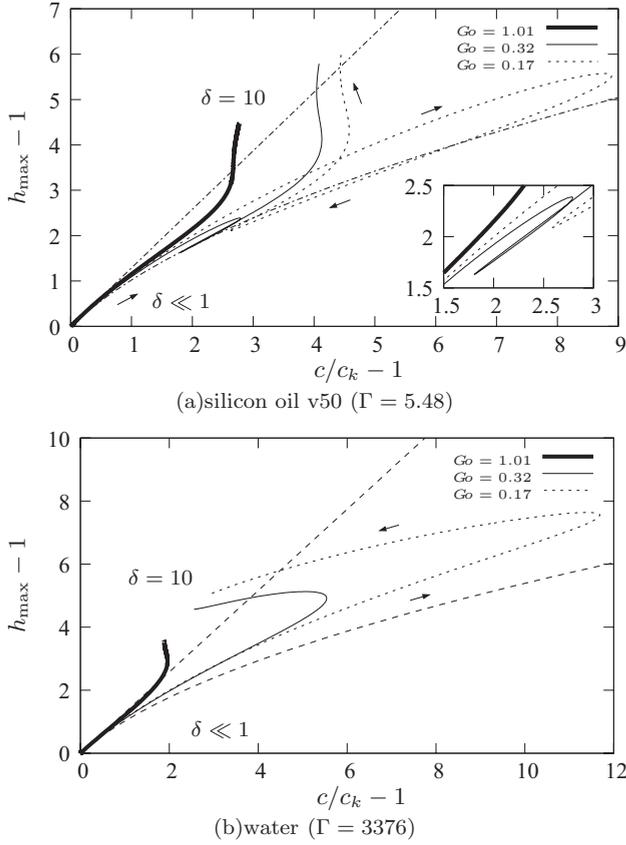
FIG. 8. Deviation wave amplitude $h_{max} - 1$ versus relative wave speed $c/c_k - 1$ for the solitary-wave solutions to (3) for Go = 1.01, 0.236, and 0.168. The dashed-dotted lines correspond to the estimates (42) and (45).

Figure 8(a) presents the dependency of $h_{max} - 1$ on the relative speed $c/c_k - 1$ for the results in Fig. 2 corresponding to the WRIBL model (3) and to silicon oil v50. The direction of increasing reduced Reynolds number δ along the curves is indicated by arrows. There is good agreement with relation (42) in the limit $c \approx c_k$. A good agreement with relation (45) is also found in the case of fast waves ($c/c_k > 6$), typical of the droplike regime observed at small Goucher numbers. In the drag-inertia regime, however, at large values of δ, the speed of the waves saturates to the limit $c_{crit}(\tilde{\alpha}, \beta/\delta)$ and no univocal mapping of the amplitude to the wave speed is observed.

When the droplike regime is affected by inertia for weakly viscous liquids, the linear relation (45) is no longer applicable reflecting the influence of the K mode on the droplike waves and in particular the steepening of the wave fronts [see Fig. 8(b)].

It is then clear from the above that Eq. (45) provides a good approximation to the speed-to-amplitude dependence for solitary waves both in the droplike and the drag-gravity regime.

V. TRAVELING WAVES

In this section, we compare periodic TW solutions of the WRIBL model (3)—that is, limit cycles of the dynamical system (14)—with ($\eta \neq 0$) and without viscous dispersion ($\eta \to 0$) and of the CM equation (5) (both $\delta \to 0$ and $\eta \to 0$)

for the experimental conditions considered in Refs. [3,5]. We revisit the description of the TWs branches of solutions given in Ref. [18] with reference to the characteristics of TWs of infinite extension, that is, as TWs approach homoclinicity. In the experimental setups of [3,5] the flow rate was controlled and maintained at a constant value at the inlet. Amplification of the ambient noise resulted in a wavy dynamics with waves traveling with constant shapes and speeds over long distances. Periodic TWs can be produced experimentally by applying periodic perturbations at the inlet [6,41]. If the signal remains periodic in time at each location in space, an integration in time of the mass balance (3a) shows that the time average of the flow rate, $T^{-1} \int_0^T q \, dt$, where T is the period, is conserved all along the fiber and is equal to its value at the inlet which gives the condition $T^{-1} \int_0^T q \, dt = 1/3$ [42]. Periodic TW solutions of the model equations aiming to describe the experimental conditions must therefore verify the condition $\langle q \rangle \equiv k/(2\pi) \int_0^{2\pi/k} q \, d\xi = 1/3$, where k again denotes the wave number.

Let us first consider the experimental conditions corresponding to the very viscous fluid considered by [3] (castor oil, $\Gamma = 0.45$; see Table I). The bifurcation diagram of TW solutions of the WRIBL model (3) and of the CM equation (5) are compared in Fig. 9(a). The parameters in the figure correspond to regime "c" reported by Kliakhandler *et al.* ($q_N = 21$ mg/s and $R = 0.25$ mm). We have normalized the wave number k with the reference $k_{RP} \equiv \sqrt{\beta}/(1 + \tilde{\alpha})$ corresponding to the marginal stability condition (real k ad ω) for linear waves solutions to the CM equation k_{RP} corresponds to a dimensional wavelength $2\pi(\bar{R} + \bar{h}_N)$ proportional to the diameter of the liquid cylinder.

Figure 9(c) shows corresponding wave profiles with regularly spaced streamlines in the moving frame, that is, isocontours of the function $\psi = \int_R^r u_x \, r \, dr + c(R^2 - r^2)/2$ at levels nq_0/N, $1 \leqslant n \leqslant N$ with $N = 10$. The surface of the fiber corresponds to $\psi = 0$ and the free surface to $\psi = q_0$. The axial velocity u_x is here computed assuming a self-similar velocity distribution corresponding to the Nusselt base flow [18]. In the case of the WRIBL model (3), only one branch of TW solutions has been found emerging from the marginal linear stability conditions at $k \approx k_{RP}$ through a Hopf bifurcation, whereas a secondary branch has also been found by period doubling for the CM equation (5). We note that weakly nonlinear TW solutions of (3) travel at a smaller speed than the TW solutions of the CM equation (5) since the speed of linear kinematic waves is significantly affected by the second-order viscous effects as emphasized in Sec. III. At small wave numbers, TW solutions of the branch emerging from $k \approx k_{RP}$ accelerate, become more and more localized, and terminate into the single-hump solitary waves discussed in Sec. III. The speed, amplitude, and shape of the solutions of (3) and (5) are comparable in this limit. Following the terminology introduced by Chang and co-workers for falling films on a planar substrate [43,44], we refer to this branch of solutions as the "γ_2 waves." The branch of solutions to (5) emerging through period doubling terminates by slow waves with a shape made of a trough followed by capillary ripples. Following again [43,44] for planar substrates, we refer to these TWs as the "γ_1 waves."
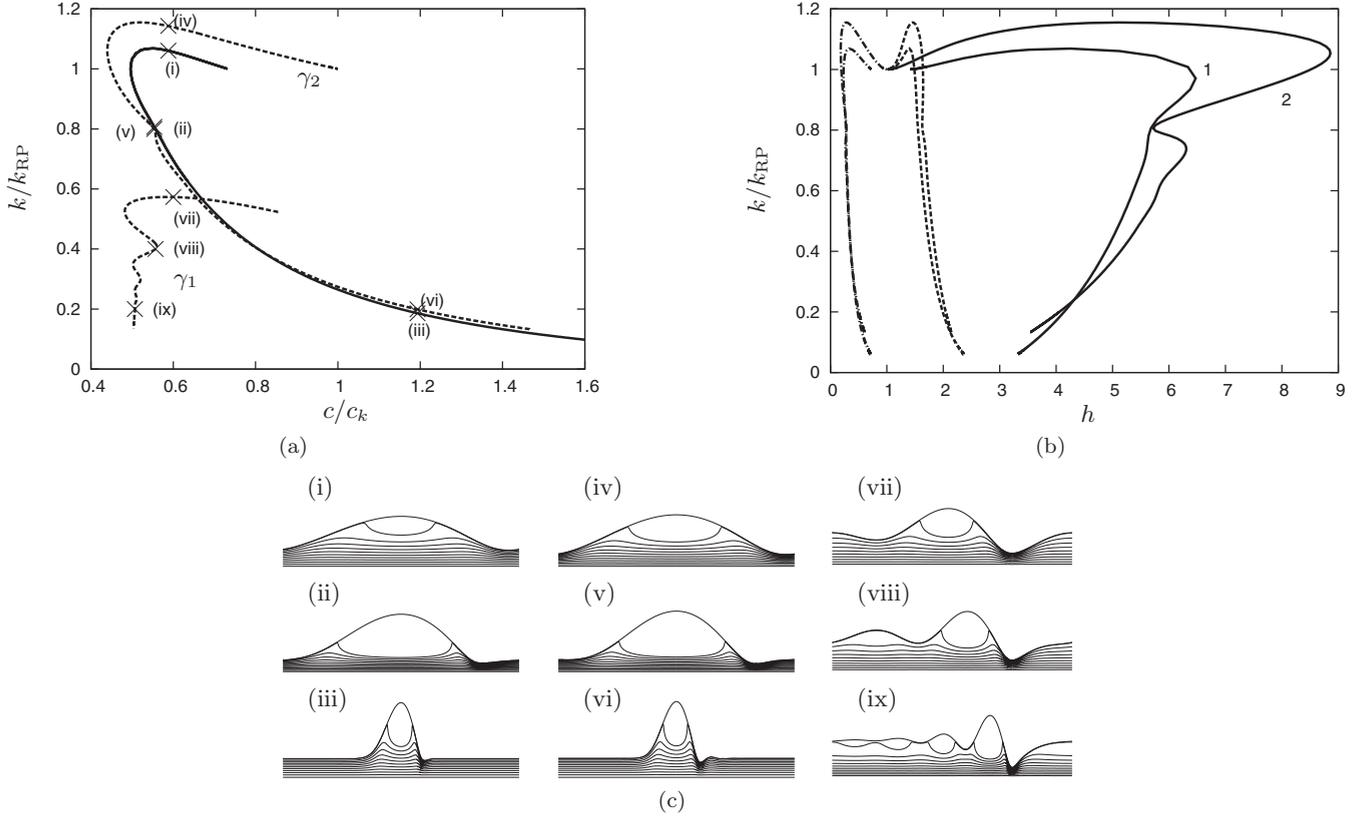
FIG. 9. TW branch of solutions bifurcating from the marginal stability conditions. (a) Normalized speed c/c_k as function of the normalized wave number k/k_{RP}, where $k_{RP} = \sqrt{\beta}/(1 + \tilde{\alpha})$ (see text). Solid and dashed lines refer to (3) and to the CM equation (5), respectively. (b) Maximum thickness h_{max} (dashed line) and substrate thickness h_s (dashed-dotted line) as functions of the normalized wave number k/k_{RP}. The solid line refers to the relative maximum thickness h_{max}/h_s. Labels 1 refer to model (3), whereas labels 2 refer to the CM equation (5). (c) Wave profiles and streamlines in the moving frame for solutions indicated by crosses in panel (a); left, solutions to (3); right, solutions to (5). Parameters correspond to the experimental conditions of [3]: $q_N = 5.3$ mg/s and $R = 0.25$ mm (Go $= 0.138$, $\tilde{\alpha} = 2.04$, $\delta = 0.01$, $\eta = 0.18$, and $\beta^{\star} = 2.1$).

For the conditions of Fig. 9, the fiber radius is small compared to the capillary length (Go $= 0.138$) and the Nusselt film thickness is comparable to the fiber radius ($\tilde{\alpha} = 2.04$). As a consequence, the RP instability mechanism is strong and TWs have amplitudes comparable to the fiber radius, which corresponds to the typical situation of the droplike regime of the solitary waves discussed in Sec. IV A. Yet, a direct transposition of the results obtained in Sec. IV A to solitarylike wave trains in the limit $k \to 0$ is not possible since the reference thickness of the substrates of the solitarylike waves is not constant (recall that in the treatment of solitary-wave solutions, the constant film thickness far from the solitary waves was the reference thickness). We have computed the parameter $\beta_s^{\star}$ based on the substrate thickness h_s (again, "substrate" refers to the base liquid film on which the waves travel) defined by the position of the fixed point in the phase space when the corresponding limit cycle approaches homoclinicity. The maximum of the relative thickness h_{max}/h_s, 6.5 here, is reached for a value of the local number $\beta_s^{\star}$ close to its maximum, namely 3.65, as expected since the waves' characteristics are piloted by the balance between the advection by the flow and the RP instability in the droplike regime. Figure 9(b) shows the evolution of the maximum thickness, h_{max}, of the substrate thickness h_s and

of the ratio of the two as function of the normalized wave number k/k_{RP}. At small k, a TW is solitarylike and travels on a portion of nearly flat substrate of increasing length. The mass transported by the wave decreases in comparison to the mass carried by the substrate and h_s asymptotes to the Nusselt film thickness. As a consequence, h_s increases as k tends to zero. This trend is followed by the maximum height h_{max}. As a TW gets more and more localized, it tends to have bigger and bigger size. However, the maximum relative thickness, h_{max}/h_s, is a rapidly decreasing function of k at small wave numbers. Indeed, larger substrate thicknesses imply weaker RP instability mechanisms and stronger advection: $\beta_s^{\star}$ (not shown) follows a trend similar to h_{max}/h_s. We therefore obtain a rather paradoxical picture: Despite the weakening of the RP instability—thus the lowering of h_{max}/h_s—a TW has its absolute amplitude augmented as k tends to zero.

For the experiments by Kliakhandler *et al.*, the RP instability mechanism is strong while inertia and viscous dispersion are weak ($\delta = 0.01$, $\eta = 0.18$), which explains the good agreement obtained with the results from the CM equation (5). However, as the RP instability is weakened by raising the Goucher number, streamwise viscous dispersion should play an increasingly important role. We have checked this by
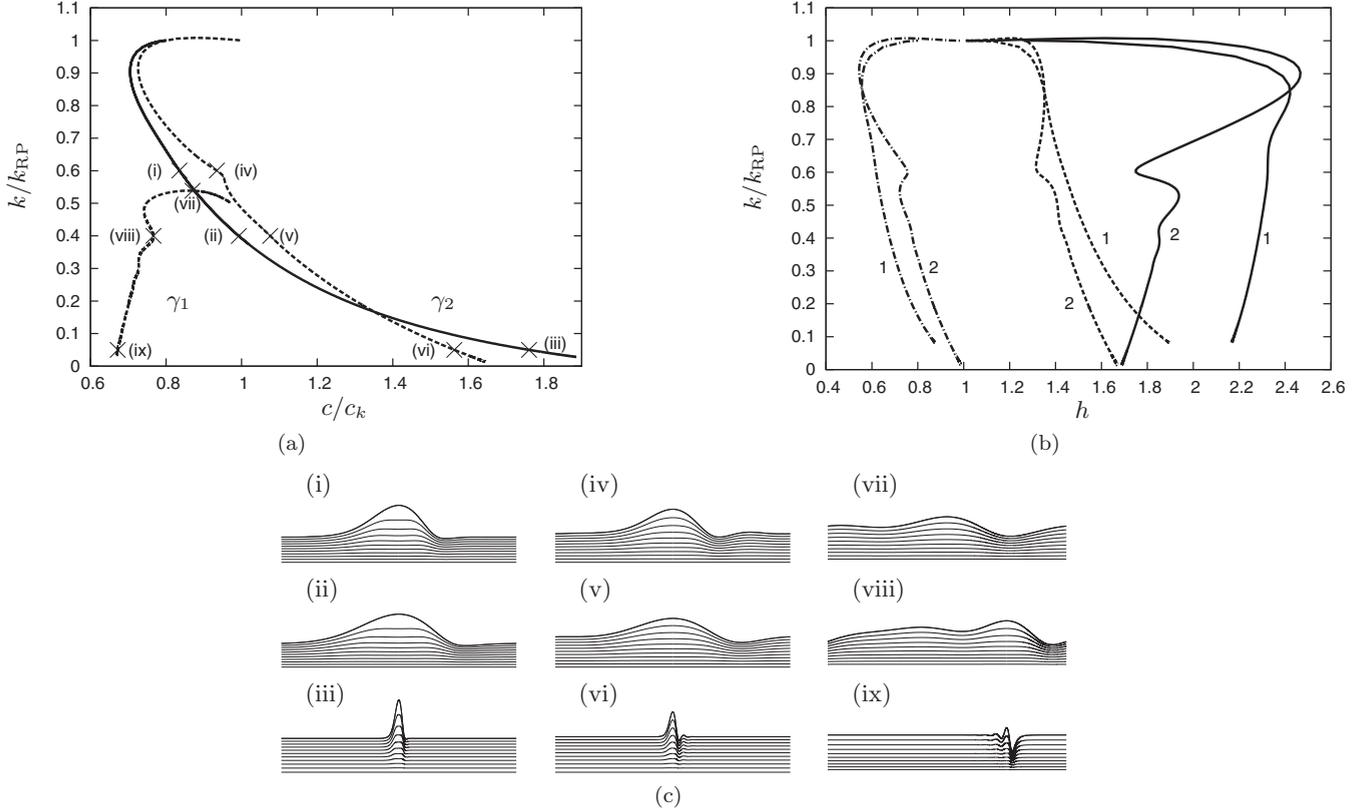
FIG. 10. TW branch of solutions bifurcating from the marginal stability conditions. Parameters correspond to castor oil ($\Gamma = 0.45$), $q_N = 10$ mg/s and $R = 0.5$ mm ($\delta = 0.01$, $\eta = 0.22$, $\tilde{\alpha} = 1.15$, and $\beta^\star = 1.16$). See caption of Fig. 9.

computing the TW solutions of (3) and (5) corresponding to a flow rate $q_N = 10$ mg/s and a larger radius $R = 0.5$ mm, that is, for $\delta = 0.01$, $\beta^\star = 1.16$, and $\eta = 0.22$, parameters that are comparable to those corresponding to the regime "c" discussed by Kliakhandler *et al.* ($\delta = 0.01$, $\beta^\star = 2,1$ and $\eta = 0.18$) but with a value of $\beta^\star \sim$ two times smaller. Branches of solutions are compared in Fig. 10(a) in the ($k/k_{RP}, c/c_k$) plane. γ_2 fast TW solutions of (5) are again observed to emerge from the marginal conditions $k \approx k_{RP}$, whereas γ_1 solutions are obtained through a period doubling bifurcation of the γ_2 branch. We note again that only the γ_2 branch of solutions can be found for the WRIBL model (3), with no period doubling bifurcation being detected in this case. We therefore conclude that the inclusion of second-order viscous effects reduces the number of wave families and, as a consequence, it may drastically simplify the complex sequence of bifurcations and topological structure of associated bifurcation diagrams. In fact, such a reduction of the number of wave families by the second-order viscous terms was also evidenced in the planar case [45].

In comparison to Fig. 9(a), the γ_2 branches portrayed in Fig. 9(a) now deviate significantly from each other even at small wave numbers. The TW solutions of model (3) have a larger amplitude than the TW solutions of equation (5) as indicated in Fig. 10 which compares the wave profiles of waves of equal wave number. When approaching homoclinicity, this effect is enhanced, and solutions of (3) travel with a notably higher speed and larger amplitude than solutions of (5). They are also preceded by smaller capillary ripples.

Figure 10(b) compares h_s and h_{max}. Again, the substrate thickness and the maximum thickness have the same trend as k tend to zero whereas the maximum relative thickness h_{max}/h_s evolves in the opposite direction. However, a comparison of Fig. 10(b) to Fig. 9(b) reveals that the maximum reached by h_{max}/h_s is approximately three times smaller than with the experimental conditions considered by [3]. Computations of the local values of the parameters based on the substrate thickness show that $\beta^\star_s$ does not exceed 1.41 and decreases with k, whereas η_s increases. The local parameters are $\beta^\star_s = 1.2$ and $\eta_s = 0.19$ for the wave profile labeled (iii) in Fig. 10 so that viscous dispersion effects start to be comparable with the RP instability mechanism. Viscous dispersion amplifies the RP instability mode by increasing the advection time τ_a, thus giving more time for the waves to grow, as already stated in Sec. III. This unexpected amplification mechanism is here very significant. The γ_2 waves computed with the WRIBL model having an amplitude that is much larger than with the CM equation [compare panels (iii) and (vi) in Fig. 10(c)].

For less viscous fluids like Rhodorsil silicon oil v50, one may expect a more significant effect of inertia and of the K mode of instability. In Fig. 11(a), we compare the substrate, maximum, and relative maximum thicknesses, h_s, h_{max}, and h_{max}/h_s, respectively, corresponding to the TW branch of solutions to (3). Parameters are chosen to correspond to one of the experimental conditions considered by [5] ($R = 0.23$ mm, $q_N = 151$ mg/s) and to a Goucher number Go $= 0.155$ close to the corresponding one for the experiments in Ref. [3] (Go $= 0.137$).
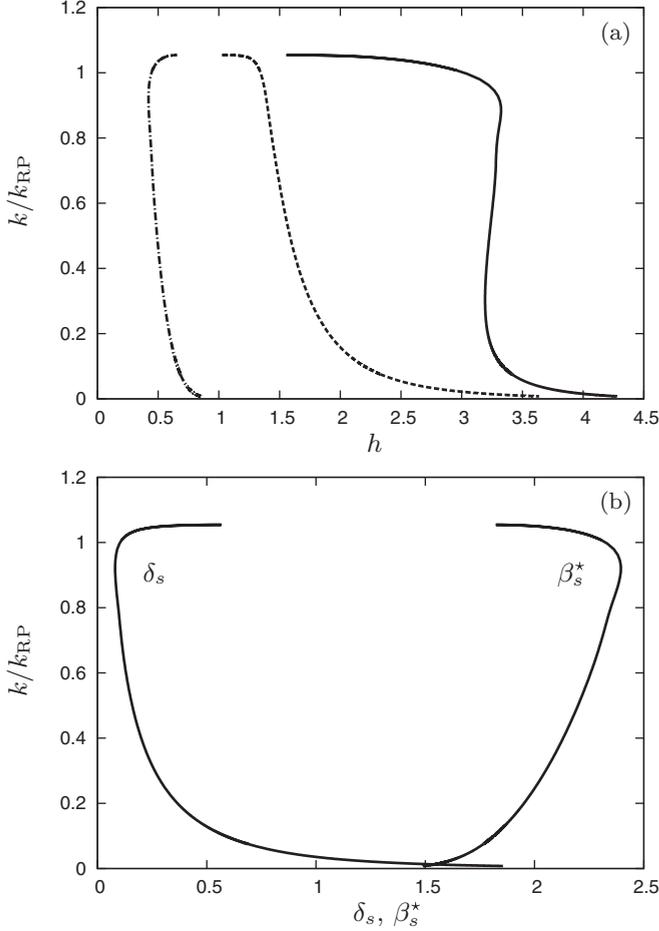
FIG. 11. (a) Maximum thickness h_{max} (dashed line) and substrate thickness h_s (dashed-dotted line) versus the normalized wave number k/k_{RP}. The solid line refers to the relative thickness h_{max}/h_s. (b) Local reduced Reynolds number δ_s and $\beta_s^\star$ versus k/k_{RP}. Parameters correspond to Rhodorsil v50 silicon oil ($\Gamma = 5.48$), $q_N = 151$ mg/s, and $R = 0.23$ mm (Go = 0.155, $\delta = 3.9$, $\tilde{\alpha} = 3.0$, and $\eta = 0.36$).

As k is lowered and the TWs approach homoclinicity, h_s and h_{max} grow, a trend similar to what is observed in Figs. 9(b) and 10(b) for a more viscous fluid. However, the relative amplitude h_{max}/h_s follows a surprising nonmonotonic behavior with an S-shape curve in the plane ($h,k/k_{RP}$). This behavior can be understood by examining the local values of δ and $\beta^\star$ based on the substrate thickness h_s and presented in Fig. 11(b). As k is lowered to zero, $\beta_s^\star$ decreases, whereas δ_s varies in the opposite direction. As a result, the two curves ultimately cross and very long waves correspond to a relatively stronger K instability mode than the initially dominant RP instability. We thus recover the usual trend observed with the solitary waves propagating on a planar film: Larger substrates imply larger amplitudes h_{max} and also larger relative amplitude h_{max}/h_s [44,46].

Interestingly, TWs can be found at a wave number k higher than the critical wave number $k_c \approx k_{RP}$ corresponding to the marginal stability conditions, in which case the Nusselt solution is linearly stable. This subcritical bifurcation of TW solutions from the Nusselt uniform film occurs at small radii

of the fiber, that is, small Goucher number (see Figs. 9 and 10). The subcritical onset of TWs has also been reported in the recent work by Novbari and Oron [47] based on an "energy integral method" though these authors did not give a physical interpretation of this phenomenon. Since the RP instability mechanism is strong when Go ≪ 1, we can conjecture that the onset of subcriticality is related to surface tension effects associated with the azimuthal curvature (hence, this effect is absent in the planar case). From a thermodynamic viewpoint, surface forces tend to reduce the free energy of the system and equilibrium is reached when the contact area between the liquid and the surrounding gas is minimum. Obviously, the flow is out of equilibrium and a thermodynamic argument must be taken with care [48]. Yet, when $\delta \ll 1$, $\eta \ll 1$, and Go ≪ 1, the WRIBL model (3) reduces at leading order to the long-wave Young-Laplace equation and the shape of the TWs thus only slightly differs from the shape of static drops on fibers as was shown in Sec. IV A and in Fig. 5.

We have computed the TW solutions to the CM equation (5) for Go = 0.02 and Go = 0.055, and for $\tilde{\alpha} = 0.5$ and $\tilde{\alpha} = 8$. (We recall that the CM equation corresponds to the inertialess $\delta \to 0$ and dispersionless $\eta \to 0$ limits of the WRIBL model for which the set of parameters reduces to $\tilde{\alpha}$ and Go.) The maximum amplitude h_{max}, and the interfacial area A of the waves normalized by the area of the uniform film solution
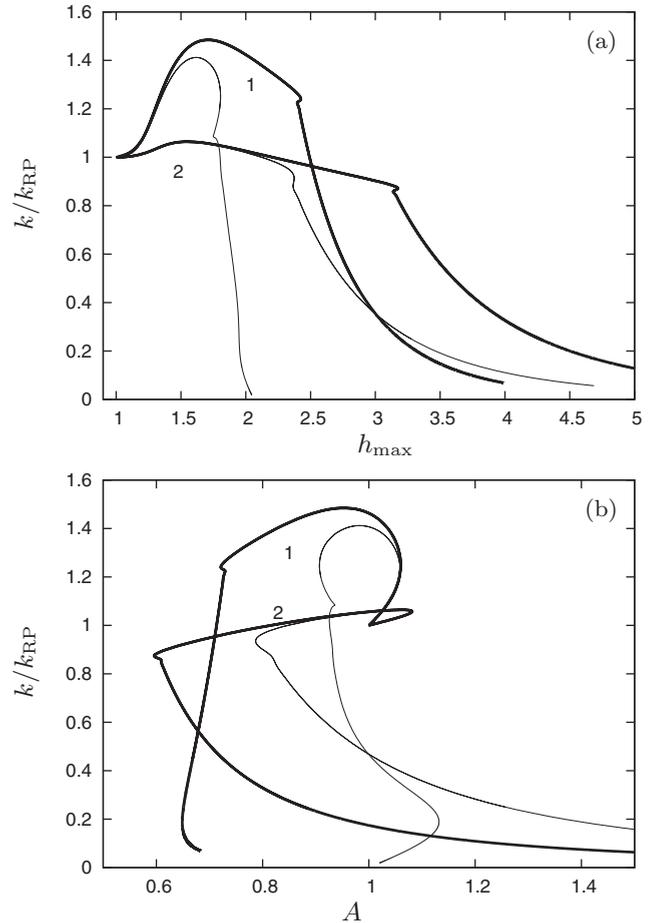
FIG. 12. TW solutions to the CM equation (5) for $\tilde{\alpha} = 8$ and $\tilde{\alpha} = 0.5$. Thick and thin solid lines refer to Go = 0.02 and Go = 0.055, respectively. Curves labeled 1 (2) correspond to $\tilde{\alpha} = 8$ ($\tilde{\alpha} = 0.5$).
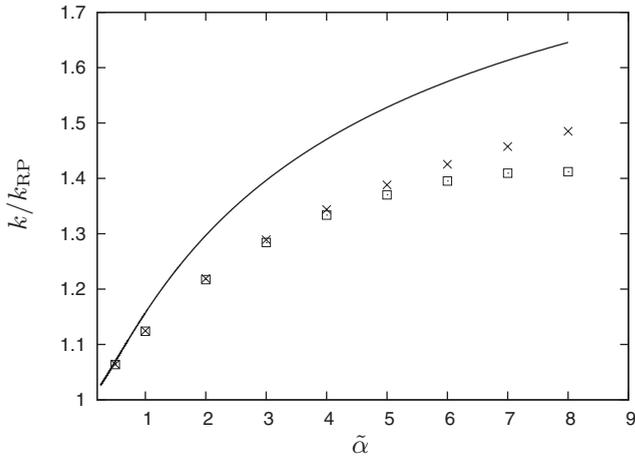
FIG. 13. Location of the maximum of the normalized wave number $k/k_{\rm RP}$ as function of the aspect ratio $\tilde{\alpha}$ for the TW solutions of the CM equation (5). Crosses (squares) correspond to Go = 0.02 (Go = 0.055). The solid line denotes the static drop solution to (B1) with a normalized area $A = 1$ (see text and Appendix B).

of the same volume are displayed in Fig. 12. The subcritical onset of the TW solutions is accompanied by a normalized interfacial area lower than unity, and therefore a lowering of the free-surface energy in comparison to the Nusselt uniform film solutions, which supports our conjecture that subcriticality is promoted by capillary effects. We note that the minimum wave number at which TWs are observed seem to depend only on $\tilde{\alpha}$ independently of Go. Conversely, at a given value of $\tilde{\alpha}$, the

amplitude of the waves is strongly affected by the value of Go, a small Goucher number implying larger waves as expected, since the saturation number $\beta = \tilde{\alpha}^{2/3}{\rm Go}^{-4/3}$ is also larger.

In Fig. 13 the maximum of the normalized wave number $k/k_{\rm RP}$ of the TW solutions of the CM equation is depicted as function of the aspect ratio $\tilde{\alpha}$ for Go = 0.02 and Go = 0.055. We note again that the location of this local maximum only weakly depends on the Goucher number. The shape of the corresponding TW solutions (not shown) is also nearly symmetrical. We thus conclude that the subcritical behavior of the TW solutions is not affected by gravity effects at small values of the Goucher number but is strongly dependent on the parameter $\tilde{\alpha}$ and therefore on the geometry of the base flow.

By neglecting gravity effects and assuming a wettable substrate, the shape of a static drop is governed by its length and volume. Therefore, for a normalized area A set to unity, the shape of a static drop depends only on the aspect ratio $\tilde{\alpha}$ of the uniform film solution with the same volume. The solid line curve in Fig. 13 represents the wave number of static drops with unit normalized areas. Above this curve, $A > 1$ and the static drop solution is not energetically favorable, whereas below it the static drop solution is favored. Indeed, large drops have a nearly spherical shape with an interfacial area that is lower than the uniform film with the same volume, with further lowering of the interfacial area being forbidden by the presence of the fiber. For a given amount of liquid, the thicker the uniform film solution is, the lower the normalized area of the static drop would be. Therefore, the range of energetically favored wave numbers of the static drop solution increases with the aspect ratio $\tilde{\alpha}$ as can be observed from Fig. 13.
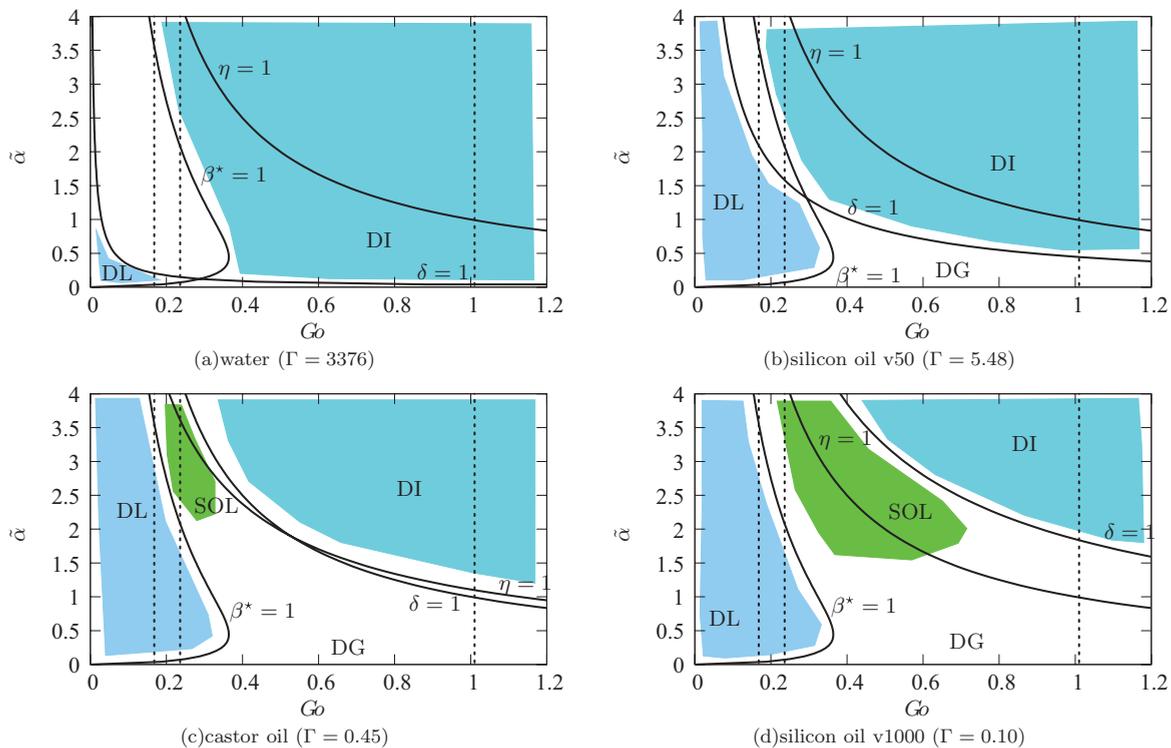
FIG. 14. (Color online) Maps of the different regimes in the Go $-\tilde{\alpha}$ parameter space for fluids of increasing viscosity. The different curves are the loci of $\delta = 1$, $\eta = 1$, and $\beta^\star = 1$. DI refers to the drag-inertia regime, DL to the Rayleigh-Plateau regime, SOL to the solitonlike regime, and DG to the drag-gravity regime.

We can now deduce two more arguments from Fig. 13 which support a capillary origin of the subcritical behavior of the branch of TW solutions that emerge from the Hopf bifurcation of the uniform film solution: (i) Since all points lie below the solid curve, TWs only exist when an energetically favorable static drop solution is available; (ii) the trend of the maximum of the TW wave number with respect to the aspect ratio $\tilde{\alpha}$ is similar to the trend of the boundary separating energetically favored and unfavored static drop solutions.

VI. PHASE DIAGRAM

We are now in a position to give a phase diagram of the different regimes found for all possible TW solutions on a film flow down a fiber. The onset of the "droplike" regime and the "drag-inertia" regime corresponds roughly to $\beta^{\star} \approx 1$ and $\delta \approx 1$. The "solitonlike" regime arises when the instability mechanisms are weak ($\delta \lesssim 1$ and $\beta^{\star} \lesssim 1$), the film is thick, $\tilde{\alpha} = O(1)$, and viscous dispersion is strong, $\eta = O(1)$. Finally, the "drag-gravity" regime is observed when all other effects are weak ($\delta \lesssim 1$ and $\beta^{\star} \lesssim 1$ and $\eta \ll 1$). Therefore, a phase diagram can be obtained for a given fluid, thus a given Kapitza number Γ, by drawing the curves $\delta = 1$, $\eta = 1$, and $\beta^{\star} = 1$ in the plane ($\tilde{\alpha}$, Go). Since $\eta = (\tilde{\alpha}\text{Go})^{4/3}$ and $\beta^{\star} = \{\tilde{\alpha}c_k(\tilde{\alpha})/[\text{Go}^2(1 + \tilde{\alpha})^4]\}^{2/3}$ are functions of $\tilde{\alpha}$ and the Goucher number only, the corresponding curves $\beta^{\star} = 1$ and $\eta = 1$ are independent of the working fluid considered. Thus, $\delta = 1$ is the only boundary that moves in the plane ($\tilde{\alpha}$, Go) when Γ is varied. Figure 14 is a tentative representation of the phase diagrams for the four working fluids considered in this study, from weakly viscous fluids like water with a high Kapitza number, $\Gamma = 3376$, to highly viscous fluids like silicon oil v1000 corresponding to a small Kapitza number, $\Gamma = 0.10$. In the case of water, a large overlap region exists for the droplike and the drag-inertia regime corresponding to a mutual reinforcement of the two K and RP instabilities. The solitonlike regime takes over at relatively high viscosities where the curve $\delta = 1$ moves below the curve $\eta = 1$.

VII. CONCLUSIONS AND DISCUSSION

We have presented new results and insights on the characteristics of axisymmetric waves propagating down a fiber. Our analysis was based on the two-equation model derived in Ref. [18] using a weighted-residuals approach [Eq. (3)]. The model accounts for all physical effects, namely inertia, azimuthal curvature, and viscous dispersion and has been validated in the studies by Ruyer-Quil *et al.* [18] and Duprat *et al.* [6] through direct comparisons to the experiments by Kliakhandler *et al.* [3] and Duprat *et al.* [5,6].

We first focused on isolated waves running on a constant thickness substrate or solitary waves. The dynamics of the film seems to be dominated by these structures even when the flow becomes disordered [3,4]. We examined in detail, via both asymptotic analysis and through elements from dynamical systems theory, the shape, speed, and amplitude of the waves for four fluids of increasing viscosities: water, Rhodorsil silicon oils v50 and v1000, and the castor oil utilized in the experiments by [3].

We identified four distinct regimes corresponding to the competition of the two instability modes, the K and RP modes, prompted by inertia and azimuthal curvature (the fiber curvature effectively), respectively, with the viscous dispersion (i.e., the second-order axial viscous diffusion and second-order viscous contributions to the tangential stress at the free surface) and with the advection of the structures by the flow, which results from the balance between gravity and viscous drag. Two of these regimes are similar to what is found in the planar geometry [10]. The drag-gravity regime corresponds to the predominance of the flow advection over the instability mechanisms, either when inertia effects are weak, that is, for $\delta \lesssim 1$ or when the azimuthal curvature effects are nondominant, $\beta^{\star} \lesssim 1$. In both cases it is possible to interpret the drag-gravity regime as one where the instability growth is arrested by the flow which determines the amplitude and speed of the solitary waves as reflected by the asymptotic relations (36). The drag-inertia regime is observed at large reduced Reynolds numbers, $\delta \gg 1$, when the wave characteristics are determined by the balance of inertia, drag, and gravity. We have obtained the asymptotic limit of the speed and showed that the rate of convergence to this limit is governed by $\eta/\delta^2 \propto \text{Re}^{-2}$.

The droplike regime corresponding to the predominance of the RP instability mechanism over the flow advection. It is specific to the cylindrical geometry and is observed for small fiber radii R compared to the capillary length l_c, that is at small Goucher numbers Go, when the typical time of growth of the RP instability is greater than the advection time of a wavy structure, that is, for $\beta^{\star} \gtrsim 1$. The maximum reachable amplitude and speed of the waves in this regime is governed by the radius R of the fiber and the balance of gravity and viscous drag. Comparisons to quasistatic drop solutions of the Laplace-Young equation (B1) sliding down a fiber with a speed verifying the Landau-Levich-Derjaguin law (B4) show excellent agreement, even in the case of spherical drops where the long-wave assumption does not strictly apply. In this regime, waves have a droplike nearly symmetrical shape determined by capillary effects. The thickness of the substrate film on which the drops slide is governed by the balance of viscosity and capillarity. Droplike TW solution branches subcritically emerge from the Nusselt uniform film branch. We have given an explanation for this subcritical onset based on geometric and thermodynamic arguments and thus completed its recent investigation in Ref. [47]. This phenomenon arises from capillary effects and depends only on the aspect ratio $\tilde{\alpha}$ for sufficiently low Goucher numbers.

We have also found a possible fourth regime for very viscous fluids and thick films ($\tilde{\alpha} = O(1)$), for which both K and RP instability mechanisms are weak ($\delta \lesssim 1$ and $\beta^{\star} \lesssim 1$) and viscous dispersion is significant ($\eta = O(1)$). This solitonlike regime corresponds to the balance of the nonlinearities with the dispersion induced by second-order viscous effects, with the speed and amplitude of the solitary waves being functions of the logarithm of the aspect ratio $\tilde{\alpha}$.

Our study of the solitary-wave solutions has been followed by construction of the TW branches of solutions corresponding to the experimental conditions for which the average flow rate is the true control parameter, with the substrate thickness being determined by the solution itself. If the substrate thickness h_s

and the maximum amplitude h_{max} grow when TWs approach homoclinicity, the ratio of the two, h_{max}/h_s, evolves in a manner that strongly depends on which instability mechanism is dominant. If the RP instability is dominant, h_{max}/h_s decreases as the wave number k tends to zero, whereas if the K mode is dominant h_{max}/h_s has an opposite trend. This picture can be even more complex since the predominance of the instability modes can be exchanged by varying the periodicity of the waves and thus the substrate thickness (cf. Fig. 11). The selected wave regime depends not only on the properties of the Nusselt flow at the inlet but also on the periodicity selected by the system. Indeed, the boundaries separating the different regimes are not only functions of Go and $\tilde{\alpha}$ but also functions of the thickness of the substrate, which is determined by the typical distance separating solitarylike waves. Therefore, the phase diagrams displayed in Fig. 14 must be taken with caution. The wave-selection process of a noise-driven falling film is the complex result of the linear amplification of inlet perturbations and the downstream nonlinear interaction mechanisms [22,50,51].

Noteworthy is that we have evidenced a nontrivial amplification mechanism of the RP instability when viscous dispersion becomes strong. This effect has been explained by a reduction of the wave speed, thus an increase of the typical time of advection τ_a of the structures. As the waves have more time to grow before reaching saturation, their amplitude becomes larger. Besides, in our previous study on the fiber problem [18], we have shown that the wave-selection process of the noise-driven wave dynamics down the fiber is strongly affected by viscous dispersion. This effect is generally weak in the experiments devoted to falling films on planar substrate, where working fluids were often weakly viscous, that is, water [40,41,52]. In the case of films down fibers, the oils used in the experiments are much more viscous than water, which explains that viscous dispersion can be dominant and can promote a solitonlike regime. In this regime and despite the dissipative nature of the flow, it is possible to observe the formation of solitons, that is, solitary waves whose shape and speed are not altered by collisions with other solitary waves (such waves are still dissipative but they share several common features with
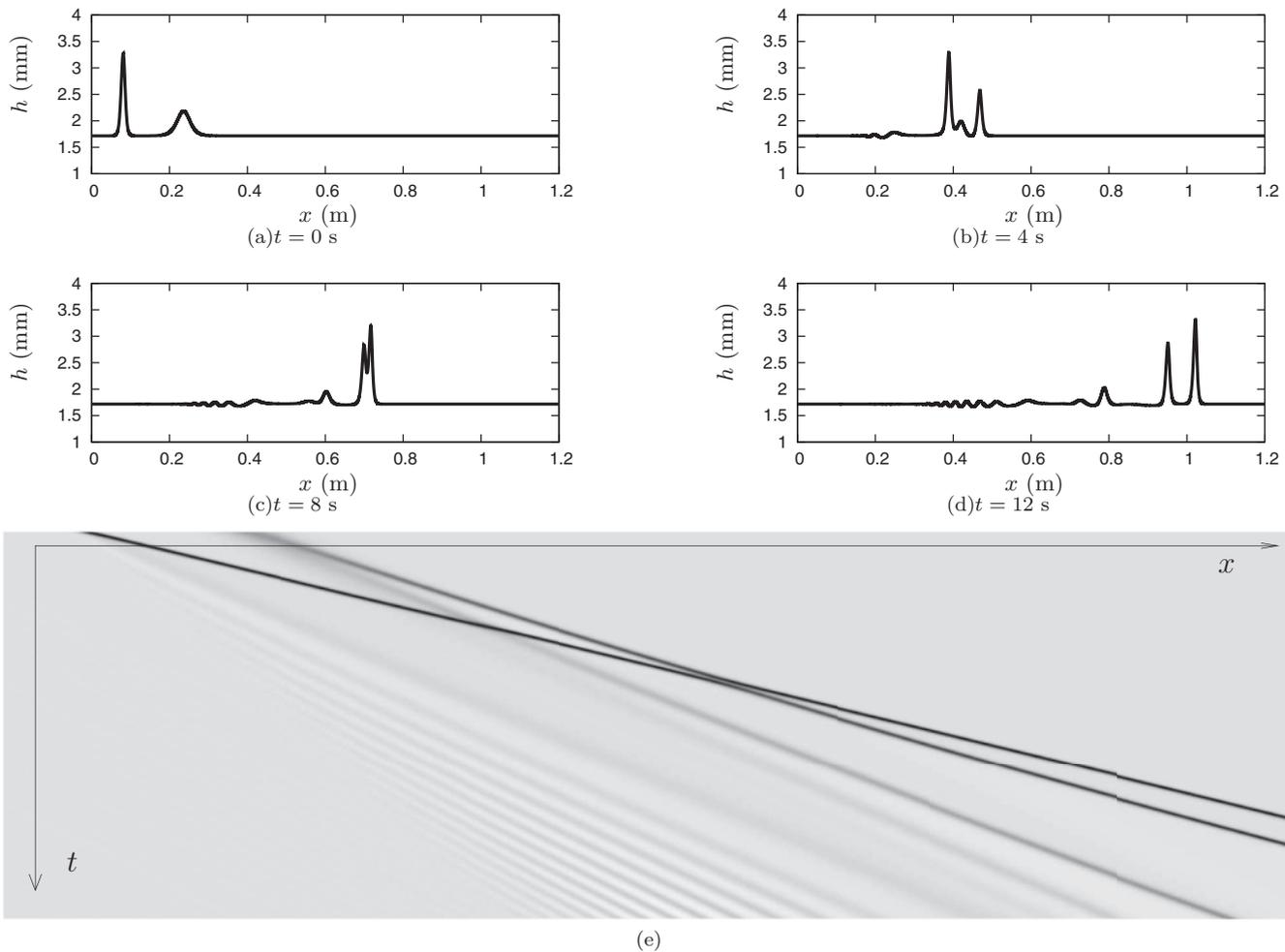
FIG. 15. Simulation of the response of the film in the solitonlike regime. Initial conditions consist of two pulselike perturbations of different amplitudes. Parameters are $\delta = 0.18$, $\tilde{\alpha} = 1.9$, and $\eta = 1.2$ (Rhodorsil silicon oil v1000, $q_N = 300$ mg/s, and $R = 0.89$ mm). (a)–(d) Snapshots of the film thickness at increasing times; (e) spatiotemporal diagram. Vertical and horizontal ranges are 1.25 m and 28 s, respectively. Elevations (depressions) of the free surface are coded in dark (light) gray.

solitons in conservative systems [53]). We explore such effects in Fig. 15 which depicts a simulation of the interaction between two solitons. Chosen parameters correspond to Rhodorsil silicon oil v1000 and Go = 0.6. Two pulselike perturbations of different amplitudes are initially placed in the computational domain (cf. panel a). The excess mass carried by these two perturbations are then drained behind the two pulses creating two wave packets. The spatial extent of these packets grows in time due to the convective instability of the film [5,18]. Panel b shows the interaction of the second pulse with the mass ejected by the first pulse. The spatiotemporal diagram shown in panel e indicates that the second pulse first overtakes this excess mass and next the first pulse without absorbing them (cf. panels c and d). The coalescence of the two pulses is accompanied by a phase shift but no notable modifications of the speeds and amplitudes of the pulses as in Hamiltonian systems: The initial wave profiles get superimposed as the waves collide and reappear as the waves move apart. Yet, a slow evolution of the amplitude and speed of the two solitons can be observed toward the speed $c = 7.5$ cm/s and amplitude $h_{\max} = 3.3$ mm of the infinite-domain solitary-wave solution for the given set of parameters (the initially larger pulse slightly reduces its amplitude, whereas the second pulse

grows by extracting energy from the substrate base film solution).

Our hope is that this new evidence of existence of solitons on a liquid film flowing down a fiber, a dissipative system as opposed to a Hamiltonian one, may motivate a renewed interest for the experimental investigation of the resulting wave dynamics and, in particular, on the role of viscous dispersion.

APPENDIX A: COEFFICIENTS OF THE MODEL (3)

The expressions of the coefficients entering the averaged momentum balance (3b) consist of ratios of polynomials in αh and $\log(1 + \alpha h)$. Introducing $b = 1 + m$, where m is the argument of the different functions, the coefficients read

$$\phi(m) = [3((4\log(b) - 3)b^4 + 4b^2 - 1)]/[16(b-1)^3], \tag{A1a}$$

$$F(m) = 3F_a(m)/[16(b-1)^2\phi(m)F_b(m)], \tag{A1b}$$

$$F_a(m) = -301b^8 + 622b^6 - 441b^4 + 4\log(b)\{197b^6 - 234b^4 + 6\log(b)[16\log(b)b^4 - 36b^4 + 22b^2 + 3]b^2 + 78b^2 + 4\}b^2 \\ + 130b^2 - 10, \tag{A1c}$$

$$F_b(m) = 17b^6 + 12\log(b)[2\log(b)b^2 - 3b^2 + 2]b^4 - 30b^4 + 15b^2 - 2, \tag{A1d}$$

$$G(m) = G_a(m)/[64(b-1)^4\phi(m)^2F_b(m)], \tag{A1e}$$

$$G_a(m) = 9b\{4\log(b)[-220b^8 + 456b^6 - 303b^4 + 6\log(b)(61b^6 - 69b^4 + 4\log(b)(4\log(b)b^4 \\ - 12b^4 + 7b^2 + 2)b^2 + 9b^2 + 9)b^2 + 58b^2 + 9]b^2 + (b^2 - 1)^2(153b^6 - 145b^4 + 53b^2 - 1)\}, \tag{A1f}$$

$$I(m) = 64(b-1)^5\phi^2/[3F_b(m)], \tag{A1g}$$

$$J(m) = 3J_a(m)/[128(b-1)^4\phi(m)^2F_b(m)], \tag{A1h}$$

$$J_a(m) = 9\{(490b^8 - 205b^6 - 235b^4 + 73b^2 - 3)(b^2 - 1)^3 + 4b^2\log(b)[2b^4\log(b)(72\log(b)(2\log(b)b^4 - 6b^4 + b^2 + 6)b^4 \\ + (b-1)(b+1)(533b^6 - 109b^4 - 451b^2 + 15)) - 3(b^2 - 1)^2(187b^8 - 43b^6 - 134b^4 + 17b^2 + 1)]\}, \tag{A1i}$$

$$K(m) = 3K_a(m)/[16b^3(b-1)^2\phi F_b(m)], \tag{A1j}$$

$$K_a(m) = 4b^4\log(b)(233b^8 - 360b^6 + 12\log(b)(12\log(b)b^4 - 25b^4 + 12b^2 + 9)b^4 + 54b^4 + 88b^2 - 15) \\ - (b^2 - 1)^2(211b^8 - 134b^6 - 56b^4 + 30b^2 - 3), \tag{A1k}$$

$$L(m) = L_a(m)/[8b(b-1)^2\phi(m)F_b(m)], \tag{A1l}$$

$$L_a(m) = 4b^2\log(b)\{6\log(b)(12\log(b)b^4 - 23b^4 + 18b^2 + 3)b^4 + (b-1)(b+1)(95b^6 - 79b^4 - 7b^2 + 3)\} \\ - (b^2 - 1)^2(82b^6 - 77b^4 + 4b^2 + 3), \tag{A1m}$$

$$M(m) = 3 + [24\log(b)b^8 - 25b^8 + 48b^6 - 36b^4 + 16b^2 - 3]/[2b^2F_b(m)]. \tag{A1n}$$

CHRISTIAN RUYER-QUIL AND SERAFIM KALLIADASISPHYSICAL REVIEW E 85, 046302 (2012)

We note that in Appendix B in Ref. [18] a small misprint can be found in the definition of the factor J—a missing factor of three—that is here corrected.

APPENDIX B: STATIC DROPS ON COATED FIBERS: COMPUTATIONS AND ASYMPTOTIC ANALYSIS

The shape of an axisymmetric drop sitting on a vertical fiber has been computed numerically by Kumar and Hartland [54] and determined analytically by Carroll [55] by neglecting gravity effects. When the contact angle of the liquid with the solid fiber vanishes, the analytical solution corresponds to an unduloid [8,56] that can be written parametrically using elliptic integrals of the first and second kind. However, the analytical solution is cumbersome to use and requires numerical evaluation of the different integrals involved. Hence, we choose to determine the solution by solving numerically the Laplace-Young equation parametrically rewritten as [54]

$$\frac{d\phi}{d\tilde{s}} = \left(\frac{d\phi}{d\tilde{s}}\right)_t + \frac{1}{R_t} - \frac{\sin\phi}{\tilde{r}}, \tag{B1a}$$

$$\frac{d\tilde{r}}{d\tilde{s}} = \cos\phi, \quad \text{and} \quad \frac{d\tilde{x}}{d\tilde{s}} = \sin\phi, \tag{B1b}$$

where the length scale is the fiber radius, $\bar{R}$. The radial and axial coordinates are denoted by $\tilde{r}$ and $\tilde{x}$, respectively. $\tilde{s}$ denotes the curvilinear arc length along the drop interface whereas ϕ is the angular inclination of the drop interface to the radial axis whereas $(d\phi/ds)_t + 1/R_t$ denotes the mean curvature at the top of the drop, $s = 0$. The set of equations is completed by the boundary conditions:

$$\phi = \pi/2, \quad \tilde{r} = R_t, \quad \tilde{x} = 0, \quad \text{at} \quad \tilde{s} = 0. \tag{B1c}$$

The contact area $\tilde{A}$ separating the liquid and gas phases and the volume $\tilde{V}$ of the drop has been computed by solving

$$\frac{d\tilde{A}}{d\tilde{s}} = 2\pi\tilde{r} \quad \text{and} \quad \frac{d\tilde{V}}{d\tilde{s}} = \pi\left(\tilde{r}^2 - R_t^2\right). \tag{B1d}$$

We have solved system (B1) using the AUTO07P software [30]. We have adjusted R_t to the coated fiber radius $1 + \tilde{\alpha}$, and the drop volume V to the volume of the corresponding solitary wave, after subtracting the volume of the residual film.

The speed of the quasistatic drops sliding on a vertical fiber can be estimated using the Landau-Levich-Derjaguin theory [57,58]. For this purpose we divide a large amplitude sliding drop in two separate regions. The "inner" one corresponding to the thin films at the upper and lower ends of the drop where viscosity balances capillary forces, and the "outer" one, the quasistatic drop itself which is governed by the Laplace-Young equation given above. In the inner region, $h \ll R$ and the equation to be solved reduces to (6), whose TW solutions are governed by

$$\frac{h^3}{3}(1 + \beta h' + h''') - c(h - 1) - 1 = 0. \tag{B2}$$

Following [14], we introduce the inner coordinates $X = c^{-1/3}\xi$ where $c \gg 1$ and get to leading order,

$$h''' = 3(h - 1)/h^3, \tag{B3}$$

the so-called "Bretherton equation" [14,59], originating from Bretherton's work on the motion of a long gas bubble in a capillary tube. In the upper region, the solution of the Bretherton equation with boundary conditions $h = 1$, $h' = h'' = 0$ at $X = 0$ is monotonic. The numerical solution of (B3) yields $\lim_{X\to\infty} h'' = 1.34$. The speed of the drops is then selected by asymptotically matching the solutions of (B1) and (B3) in the upper overlap region between inner and outer domains. This can be easily done by imposing that the Laplace pressures corresponding to the two solutions are equal in this region, giving

$$\left(\frac{d\phi}{d\tilde{s}}\right)_t + \frac{1}{R_t} = 1 + 1.34\frac{Ca^{2/3}}{\tilde{\alpha}}, \tag{B4}$$

where $Ca = c_{drops}Bo = \mu\bar{c}_{drops}/\sigma$ in the limit $\tilde{\alpha} \ll 1$.

[1] S. Kalliadasis, C. Ruyer-Quil, B. Scheid, and M. G. Velarde, Falling Liquid Films, 1st ed., Applied Mathematical Sciences, Vol. 176 (Springer, Berlin, 2012).
[2] D. Quéré, Europhys. Lett. 13, 721 (1990).
[3] I. L. Kliakhandler, S. H. Davis, and S. G. Bankoff, J. Fluid Mech. 429, 381 (2001).
[4] R. V. Craster and O. K. Matar, J. Fluid Mech. 553, 85 (2006).
[5] C. Duprat, C. Ruyer-Quil, S. Kalliadasis, and F. Giorgiutti-Dauphiné, Phys. Rev. Lett. 98, 244502 (2007).
[6] C. Duprat, C. Ruyer-Quil, and F. Giorgiutti-Dauphiné, Phys. Fluids 21, 042109 (2009).
[7] P. L. Kapitza and S. P. Kapitza, in Collected Papers of P. L. Kapitza (1965), edited by D. T. Haar (Pergamon, Oxford, 1949), pp. 690–709 [original paper in Russian: Zh. Ekper. Teor. Fiz. 19, 105–120].
[8] J. Plateau, Statique Expérimentale et Théorique des Liquides Soumis aux seules Forces Moléculaires (Gauthier Villars Paris, 1873).
[9] L. Rayleigh, Proc. London Math. Soc. 10, 4 (1878).
[10] T. Ooshida, Phys. Fluids 11, 3247 (1999).
[11] C. Ruyer-Quil and P. Manneville, J. Fluid Mech. 531, 181 (2005).
[12] A. Frenkel, Europhys. Lett. 18, 583 (1992).
[13] Y. Y. Trifonov, AIChE J. 38, 821 (1992).
[14] S. Kalliadasis and H.-C. Chang, J. Fluid Mech. 261, 135 (1994).
[15] R. V. Roy, A. J. Roberts, and A. J. Simpson, J. Fluid Mech. 454, 235 (2002).
[16] A. J. Roberts and Z. Li, J. Fluid Mech. 553, 33 (2006).
[17] E. Novbari and A. Oron, Phys. Fluids 21, 062107 (2009).
[18] C. Ruyer-Quil, P. Treveleyan, F. Giorgiutti-Dauphiné, C. Duprat, and S. Kalliadasis, J. Fluid Mech. 603, 431 (2008).
[19] A. Oron, O. Gottlieb, and E. Novbari, Eur. J. Mech. B/Fluids 28, 1 (2009).
[20] Following the terminology introduced in Refs. [23–25], a film flow model is consistent at $O(\epsilon^n)$ when all neglected terms are of higher order, or equivalently no terms of $O(\epsilon^n)$ or smaller have been omitted, and hence a gradient expansion of the model

046302-22

up to $O(\epsilon^n)$ agrees exactly with the single evolution equation for h at $O(\epsilon^n)$ obtained with just the long-wave approximation.

[21] C. Duprat, F. Giorgiutti-Dauphiné, D. Tseluiko, S. Saprykin, and S. Kalliadasis, Phys. Rev. Lett. **103**, 234501 (2009).

[22] M. Pradas, D. Tseluiko, and S. Kalliadasis, Phys. Fluids **23**, 044104 (2011).

[23] C. Ruyer-Quil and P. Manneville, Eur. Phys. J. B **6**, 277 (1998).

[24] C. Ruyer-Quil and P. Manneville, Eur. Phys. J. B **15**, 357 (2000).

[25] C. Ruyer-Quil and P. Manneville, Phys. Fluids **14**, 170 (2002).

[26] D. Quéré, Annu. Rev. Fluid Mech. **31**, 347 (1999).

[27] V. Ya. Shkadov, Izv. Akad. Nauk SSSR, Mekh. Zhidk. Gaza **1**, 63 (1977).

[28] H.-C. Chang and E. A. Demekhin, J. Fluid Mech. **380**, 233 (1999).

[29] A. Pumir, P. Manneville, and Y. Pomeau, J. Fluid Mech. **135**, 27 (1983).

[30] E. Doedel, A. R. Champneys, T. F. Fairgrieve, Y. A. Kuznetsov, B. Sandstede, and X.-J. Wang, AUTO97: *Continuation and Bifurcation Software for Ordinary Differential Equations*, Technical Report (Department of Computer Science, Concordia University, Montreal, Canada, 1997) (available by FTP from ftp.cs.concordia.ca in directory pub/doedel/auto).

[31] G. B. Whitham, *Linear and Nonlinear Waves* (Wiley-Interscience, New York, 1974).

[32] S. D. R. Wilson, J. Eng. Math. **16**, 209 (1982).

[33] H. A. Thomas, in *Proceedings of the Hydraulics Conference* (University of Iowa, Iowa City, IA, 1939), pp. 214–229.

[34] Q. Q. Liu, L. Chen, J. C. Li, and V. P. Singh, J. Hydrologic Eng. **10**, 110 (2005).

[35] T. Kawahara, Phys. Rev. Lett. **51**, 381 (1983).

[36] T. Kawahara and S. Toh, Phys. Fluids **31**, 2103 (1988).

[37] D. Tseluiko, S. Saprykin, and S. Kalliadasis, Proc. Est. Acad. Sci. **59**, 139 (2010).

[38] D. Tseluiko, S. Saprykin, C. Duprat, F. Giorgiutti-Dauphiné, and S. Kalliadasis, Physica D **239** (2010).

[39] H.-C. Chang, Phys. Fluids **29**, 3142 (1986).

[40] J. Tihon, K. Serifi, K. Argyiriadi, and V. Bontozoglou, Exp. Fluids **41**, 79 (2006).

[41] J. Liu and J. P. Gollub, Phys. Fluids **6**, 1702 (1994).

[42] B. Scheid, C. Ruyer-Quil, U. Thiele, O. A. Kabov, J. C. Legros, and P. Colinet, J. Fluid Mech. **527**, 303 (2005).

[43] H.-C. Chang, E. A. Demekhin, and D. I. Kopelevitch, J. Fluid Mech. **250**, 433 (1993).

[44] H.-C. Chang and E. A. Demekhin, *Complex Wave Dynamics on Thin Films*, edited by D. Möbius and R. Miller (Elsevier, Amsterdam, 2002).

[45] C. Ruyer-Quil, Ph.D. thesis, École polytechnique, LadHyx, France, 1999.

[46] S. V. Alekseenko, V. E. Nakoryakov, and B. G. Pokusaev, *Wave Flow in Liquid Films*, 3rd ed. (Begell House, New York, 1994).

[47] E. Novbari and A. Oron, Phys. Fluids **23**, 012105 (2011).

[48] Indeed, Kapitza himself erroneously predicted the instability threshold of a falling film using thermodynamic arguments [49], a question that was settled with Benjamin's work a few years later [60].

[49] P. L. Kapitza, *Collected Papers of P. L. Kapitza (1965)*, edited by D. Ter Haar (1948), p. 662.

[50] H.-C. Chang, E. Demekhin, and E. Kalaidin, J. Fluid Mech. **294**, 123 (1995).

[51] S. Kalliadasis and U. Thiele, *Thin Films of Soft Matter*, CISM Courses and Lectures No. 490 (Springer-CISM, Wien, 2007).

[52] S. V. Alekseenko, V. Y. Nakoryakov, and B. G. Pokusaev, AIChE J. **31**, 1446 (1985).

[53] C. I. Christov and M. G. Velarde, Physica D **86**, 323 (1995).

[54] A. Kumar and S. Hartland, J. Colloid Interface Sci. **124**, 67 (1988).

[55] B. J. Carroll, J. Colloid Interface Sci. **57**, 488 (1976).

[56] C. Delaunay, J. Math. Pures Appl. **6**, 309 (1841).

[57] L. D. Landau and B. V. Levich, Acta Physicochim. USSR **17**, 42 (1942).

[58] B. V. Derjaguin, Acta Physicochim. USSR **39**, 13 (1943).

[59] F. P. Bretherton, J. Fluid Mech. **10**, 166 (1961).

[60] T. B. Benjamin, J. Fluid Mech. **2**, 554 (1957).